Mineralium Deposita
https://doi.org/10.1007/s00126-026-01468-x

ARTICLE

Sulphides to weathering products: metal evolution in seafloor massive sulphide deposits at the Semenov hydrothermal cluster, Mid-Atlantic Ridge

Christian S. Bishop[1,2,3] · Pierre Josso[3] · Anna Lichtschlag[2] · Stephen Roberts[1] · Thomas M. Belgrano[4] · J. Andy Milton[1] · Maxime Lesage[5] · Bramley J. Murton[2]

Received: 21 August 2025 / Accepted: 8 June 2026

Abstract

Seafloor massive sulphide (SMS) deposits are potential sources of Cu, Zn, Au and Ag, however, how seafloor weathering affects the content of these metals in the deposits remains poorly understood. Key sulphide weathering products, i.e. Fe-oxyhydroxide and atacamite, can provide insight into metal mobilisation during and after oxidation of sulphides. Ten Fe-oxyhydroxide and three massive sulphide samples from the Semenov hydrothermal cluster (13°30′N, Mid-Atlantic Ridge) were studied; five Fe-oxyhydroxides and all sulphides were analysed by LA-ICP-MS with one sulphide sample analysed by LA-TOF-ICP-MS mapping. Additionally, a sequential leaching study comprising nine Fe-oxyhydroxide samples was performed. Copper is mainly sequestered into the sulphide weathering products atacamite (~60%) and Fe-oxyhydroxide (~30%). Initially, Fe-oxyhydroxide precipitates as ferrihydrite, inheriting the metal content of its sulphide precursor (e.g., pyrite or chalcopyrite). Concurrently, Au and Ag are displaced from the sulphide and become concentrated along the oxidation front at the sulphide rims rather than being incorporated into the nascent Fe-oxyhydroxide. As oxidation proceeds, further breakdown of sulphides such as chalcopyrite, releases Cu that initially adsorb onto existing Fe-oxyhydroxide. When sufficient mobilised Cu reacts with oxygenated seawater, atacamite precipitates, sequestering the Cu in a stable mineral form, serving as an exploration indicator for Cu-rich Fe-oxyhydroxide deposits and underlying massive sulphide deposits. Complete sulphide oxidation leads to the loss of Au and Ag from the solid system into seawater or their migration downwards toward a redox boundary within the SMS mound. Crystallisation of ferrihydrite into more stable goethite liberates substantial amounts of Cu (92%) and Zn (57%). However, the metal loss caused by this process may be limited if released metals re-adsorbed onto adjacent Fe-oxyhydroxide. These results reveal that Fe-oxyhydroxides can act as effective long-term traps for Cu and Zn, suggesting that older, fully or partially oxidised off-axis SMS deposits may retain considerable base metals, expanding exploration areas.

Keywords Fe-oxyhydroxide · Weathering · Metal mobility and redistribution · Seafloor massive sulphide deposits · Mid-Atlantic Ridge · LA-ICP-MS

Editorial handling: K. Kelley

✉ Christian S. Bishop
csb1u21@soton.ac.uk; cbish@bgs.ac.uk

[1] School of Ocean and Earth Science, University of Southampton, Southampton, UK

[2] National Oceanography Centre, Southampton, UK

[3] Present address: British Geological Survey, Keyworth, Nottingham NG12 5GG, UK

[4] UCD School of Earth Sciences, University College Dublin, Belfield Dublin 4, Ireland

[5] Nedre Slottsgate 8, Oslo 0157, Norway

Introduction

Weathering of sulphides on the seafloor redistributes base and precious metals and can significantly modify the geochemical signature of seafloor massive sulphide (SMS) deposits. The behaviour of base and precious metals during sulphide oxidation is well-documented in terrestrial systems, where oxidation of sulphides with meteoric fluid generates acidic fluids, which mobilise redox-sensitive metals like Cu and Zn and can concentrate residual precious metals like Au and Ag to form supergene deposits (Emmons 1917;

Published online: 19 June 2026

Yesares et al. 2014). For submarine settings, where seawater provides an essentially unlimited source of fluid that buffers pH to near neutrality, studies of metal mobilisation are still rather limited. This is particularly true for research on the formation and subsequent modification of sulphide weathering products like Fe-oxyhydroxide (FeOOH) and atacamite ($CuCl_2(OH)_3$; Dekov et al. 2011; Fallon et al. 2017; Melekestseva et al. 2020; Hu et al. 2022; Maslennikov et al. 2023; Hou et al. 2024). At SMS deposits, FeOOH may form either as metal-poor primary precipitates from low-temperature hydrothermal fluids or as metal-rich secondary products through sulphide oxidation (Hekinian et al. 1993). Both FeOOH and atacamite can serve as important repositories for economic metals. Atacamite is rich in Cu, while FeOOH can be enriched in Cu, Zn, Au and Ag through lattice substitution or adsorption, potentially acting as a trap for these metals following sulphide oxidation (Herzig et al. 1991; Cornell and Schwertmann 2003; Dekov et al. 2011; Melekestseva et al. 2020; Hu et al. 2022). Despite the economic relevance of FeOOH, the geochemical relationship between FeOOH and its sulphide precursor remains poorly understood (Blowes et al. 2003; Hu et al. 2023; Hou et al. 2024). If oxidised products retain the geochemical fingerprint of their sulphide precursors, they could serve as seafloor indicators of metal-rich sulphide at depth. While Au and Ag can be incorporated in sulphide inclusions in FeOOH, the fate of these metals after complete sulphide oxidation and whether they are lost to seawater or retained within FeOOH, remains uncertain (Melekestseva et al. 2020; Maslennikov et al. 2023).

It also remains unclear how the geochemical composition of FeOOH exposed on the seafloor evolves over time (Hu et al. 2022). Metastable ferrihydrite is the initially formed FeOOH mineral, which can dissolve and reprecipitate as more stable goethite crystals (α–FeOOH; Schwertmann and Murad 1983; Grundl and Delwiche 1993). This transformation could result in the loss of economic metals like Cu and Zn (Vu et al. 2013; Sajih et al. 2014), but this process has not been investigated using natural samples, requiring targeted geochemical analysis to understand metal partitioning during mineral transformation. Alternatively, post-formational modification can also enrich economic metals (i.e., Cu, Zn, Au, Ag) in FeOOH through atacamite veining or the adsorption of metals onto FeOOH derived from underlying sulphide weathering (Herzig et al. 1991; Hu et al. 2022). Finally, the deportment of Cu and Zn within these alteration products and whether they are mostly held in ferrihydrite, goethite or atacamite is unknown. Understanding the mobilisation of metals from sulphide and incorporation into weathering products, and the mechanisms of post-formational modification are essential to determine the long-term metal content of FeOOH and predict metal retention in older, extinct off-axis SMS deposits.

This study investigates sulphide weathering at the Semenov hydrothermal cluster, an ultramafic and mafic-hosted Mid-Atlantic Ridge SMS system, to understand whether complete oxidation of sulphides by seawater results in a metal-poor deposit or if alteration products, such as FeOOH and atacamite, retain the economic metals. The specific objectives are: (1) to examine the oxidation pathways of different sulphide minerals and the accumulation of Cu, Zn, Au, and Ag in the weathering products; (2) to assess how post-formational modifications, such as seawater interaction and goethite crystallisation, alter the composition of FeOOH; and (3) the implications of SMS weathering products as a potential resource at SMS deposits.

Geological setting

Situated along the western margin of the Mid-Atlantic Ridge at 13°30'N, the Semenov hydrothermal cluster lies on a striated dome oceanic core complex characterised by east-west trending morphology (Pertsev et al. 2012; MacLeod et al. 2009). This elongated feature extends 10 km in length and 4.5 km in width at depths of 2480–2950 m below sea level (Fig. 1; Beltenev et al. 2007, 2009; Smith et al. 2006, 2008). Semenov hydrothermal cluster comprises five hydrothermal zones spanning from the active Semenov-2 system to extinct fields that ceased activity over 120 ka (Kuznetsov et al. 2011; Cherkashov et al. 2017). Semenov-4 was active over the longest timespan (123.8–1.7 ka), Semenov-1 shows intermediate ages (37.4–12.9 ka), and Semenov-5 represents a recently extinct system (8–14 ka). Mineralogical assemblages of the Semenov sulphides predominantly consist of Fe-sulphides (pyrite, pyrrhotite, marcasite) and Cu-sulphides (chalcopyrite, isocubanite) occurring as massive sulphides, breccias, and preserved chimney structures (Beltenev et al. 2009; Melekestseva et al. 2014, 2018; Firstova et al. 2019). Secondary alteration includes covellite, atacamite, FeOOH, and jarosite (Melekestseva et al. 2014, 2017; Bishop et al. 2025a). The host rock compositions includes ultramafic and mafic lithologies (harzburgites, gabbros, plagiogranites, tonalites, diorites, basalts; Pertsev et al. 2012).

Materials and methods

The following section provides a summary of the methods used in this study. Full methodological details are available in electronic supplementary materials (ESM) 1.1 and ESM 1.2.

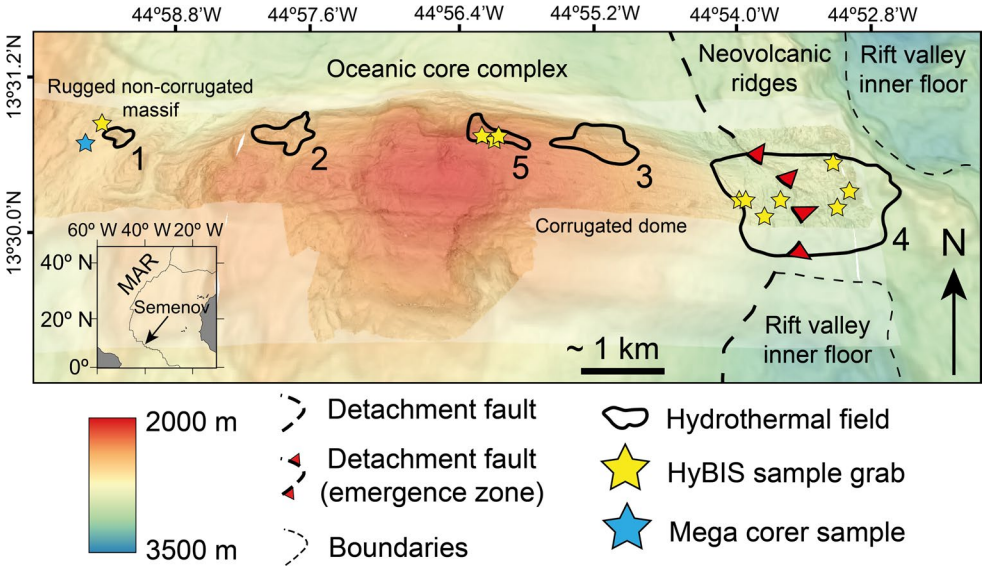

Fig. 1 1.5x vertical exaggeration 3D bathymetry map of Semenov illustrating major tectonic features and the location of hydrothermal mounds. The inset image shows the regional location of Semenov on the Mid-Atlantic Ridge (MAR). Bathymetry after Escartin et al. (2014), with tectonic settings, boundaries and location of hydrothermal mounds after Firstova et al. (2022) and Pertsev et al. (2012). The oceanic core complex is made up of the corrugated dome and the rugged non-corrugated massif. Numbers represent a hydrothermal cluster (i.e., 1 is Semenov-1 and so on)

Sample collection

Ten samples of FeOOH and three massive sulphides samples were collected from the Semenov hydrothermal cluster during the NERC-funded "ULTRA" programme expedition JC224 (RRS James Cook, March–April 2022). Seafloor samples were collected using the HyBIS robotic underwater vehicle (Murton et al. 2012; Figs. 1, 2 and 3) and a mega corer. Samples of FeOOH were collected from Semenov-1, Semenov-4 and Semenov 5, with massive sulphide samples obtained at Semenov-4 and Semenov-5 (Fig. 1). A full list of sample locations and description can be found in ESM 2 and after Bishop et al. (2025b).

Mineralogical characterisation

The samples were cut into blocks and polished for reflected light microscopy and subsequent analysis. To provide mineral quantification, previously acquired X-ray diffraction (XRD) results after Bishop et al. (2025c) were processed using Siroquant v5.2 (supplied by Sietronics Pty Ltd©). Ferrihydrite is difficult to quantify by XRD; therefore, the amorphous fraction determined using corundum as an internal standard was assumed to correspond to ferrihydrite. Amorphous content was quantified using an internal standard and interpreted to be ferrihydrite. To provide quantitative major geochemical data (>0.1 wt%), nine polished blocks were selected for quantitative scanning electron microscope-energy dispersive X-ray spectroscopy (SEM-EDS) analysis. The data collected by SEM-EDS were also used to identify targets for laser ablation time-of-flight inductively coupled plasma mass spectrometry (LA-TOF-ICP-MS) and to provide in-situ compositional information that was used for subsequent quantification of laser ablation analyses ('internal correction').

Sequential leaching procedure

Leaching experiments were conducted on nine FeOOH samples to investigate Cu and Zn distribution within sulphide weathering products, following the methodology adapted from Poulton and Canfield (2005). The four leaching solutions targeted sequentially (1) easily adsorbed fractions (using 1 M magnesium chloride buffered to pH 7), (2) carbonates and atacamite (using 1 M Na-acetate at pH 4.5), (3) ferrihydrite (using 1 M hydroxylamine-hydrochloride with 25% acetic acid), and (4) goethite (using 0.5 g/l Na-dithionite buffered with 0.2 M Na-citrate and 0.35 M acetic acid).

Geochemical analysis

LA-TOF-ICP-MS elemental mapping

Two semi-quantitative 1mm^2 trace elemental maps at 2 µm x 2 µm resolution were produced by LA-TOF-ICP-MS to investigate the distribution of metals during sulphide weathering. The analytical methodology and instrumentation (a Nu Vitesse LA-TOF-ICP-MS and ESL NWR193 laser ablation system) is detailed in Standish et al. (2024), here adapted for analysis of sulphides. The analyses were performed by ablating a 1 mm x 1 mm grid comprised of 2 µm x 2 µm square spots at a repetition rate of 400 Hz with a fluence of 3.0 J/cm^2. Instrument tuning was performed using a NIST SRM 610 glass. Calibration was achieved using standard-sample bracketing of NIST SRM 610 and United States

Geological Survey (USGS) basalt glass reference material GSD-2G. Data reduction was performed in iolite4 using the 3D Trace Elements data reduction scheme, making use of all three reference materials (Paul et al. 2023). NIST SRM 612 was used as a secondary reference material for the elements presented in this study (Cd, Cu, As, Ag and Au). At the 2 µm x 2 µm scale, results were within 10% of reference values, except for Cd (-54%), Au (-53%) and As (+35%). These are known to exhibit heterogeneity in this glass material (Eggins and Shelley 2002). During rastering of NIST SRM 612, most elements exhibit precision expressed as % relative standard deviation (RSD) better than 10.0%, except for Cu (12.0%) and Au (11.1%).

LA-ICP-MS spot analysis

Spot analysis by LA-ICP-MS (Agilent 8900 ICP-MS and ESL NWR193 laser ablation system) was used to obtain compositional data across the spectrum of fresh to weathered minerals used in this study. The data obtained were calibrated using USGS basalt glass reference material GSD-1G alongside nano-powder pellets prepared from OREAS-993 (sulphide-rich Cu concentrate certified reference material, OREAS, Australia) and Fe-Mn oxide materials JMn-1 (Geological Survey of Japan), Nod-A-1 (USGS) and FeMnOx-1 (Jochum et al. 2016). Nano-powder pellets were produced at the University of Southampton following a method adapted from Garbe-Schönberg and Müller (2014). This included milling 1.5 g batches of the starting powders in a 45 mL agate vial with 32 g of 5 mm agate balls and 6–8 g of ultrapure Milli_Q water at 900 rpm for 30 min total milling time in a Fritsch (Germany) Pulverisette 7PL™ planetary ball mill. Nano-powder slurries were then dried at 60˚C overnight, re-homogenised in an agate pestle and mortar before pressing into 13 mm diameter pellets using a Specac (UK) stainless steel die, with the back surface of the pellet stabilised by a layer of microcrystalline cellulose (~0.2 g; Merck, Germany). Quantitative SEM-EDS elemental analyses for the majority of spots analysed by LA-ICP-MS were employed as an internal standard reference for full quantification. For chalcopyrite, pyrite, and FeOOH, Fe was used as the internal standard, whereas Cu was used for atacamite. Where SEM-EDS data were unavailable, stoichiometric concentrations, Fe for pyrite and chalcopyrite, and Cu for atacamite, were applied, and for FeOOH, the average Fe composition of FeOOH analysed by SEM-EDS within the sample was used (ESM 3.1). Sphalerite was not measured by LA-ICP-MS due to its fine grain size. The reference materials used for calibrating each element are detailed as follows: Al, Si, Ca, Mn, Fe, Co, Ni, Cu, Zn, As, Se, Mo, Ag, Cd, In, Sb, Te, La, Ce, Pr, Nd, Sm, Eu, Gd, Tb, Dy, Er, Yb, Au, Pb, and Bi were calibrated using GSD-1G, Nod-A-1, and FeMnOx-1. JMn-1 was used in addition to previous certified reference material to calibrate Si, Se, Mo, Ag, Cd, In, Pb, and Bi, while OREAS-993 was employed to further calibrate Al, Ca, Mn, Co, Ni, Cu, Zn, As, Sb, Te, La, Ce, Pr, Nd, Sm, Eu, Gd, Tb, Dy, Er, Yb, Au, Pb, and Bi. The accuracy and precision of the analyses were determined for each analyte using secondary reference materials that were measured as unknowns: OREAS-993 was used as secondary reference material for Si, Se, Mo, Ag, Cd, In, Pb and Bi with JMn-1 used as the secondary reference material for Al, Ca, Mn, Co, Ni, Cu, Zn, As, Sb, Te, La, Ce, Pr, Nd, Sm, Eu, Gd, Tb, Dy, Er, Yb and Au. Using either OREAS-993 and JMn-1 as secondary reference materials achieved the highest accuracy and precision for the measured elements. The majority of elements exhibit good precision and accuracy with concentrations within the reported uncertainty or within 10% of reference values, except for Si (33.3%), Zn (18.6%) and Cd (61%). The majority of elements exhibit %RSD of < 10%, except for Au (17.1%). See ESM 1.3 for a full record of quality control checks.

Leachate analysis by ICP-MS and ICP-OES

The filtered solutions acquired from the sequential leaching experiments were analysed by solution ICP-MS and ICP optical emission spectrometry (ICP-OES) for their major and trace element concentrations. Measurements were calibrated against synthetic standards of known concentrations. Accuracy and reproducibility of the analyses were assessed by analysing reference materials JMn-1 (USGS), GSPN-2 (Mn nodule, Chinese Academy of Sciences), RTS-1 (Sulphide ore, CANMET), in triplicate and further single analyses of Nod-P-1, GSPN-3 (Mn nodule, Chinese Academy of Sciences), and CH-4 (Au ore, CANMET). Most elements exhibit accuracy within 7% of the reference values, except for Zn (-32.3%) and Ca (9.6%; see ESM 1.4 for full details). Analysed elements exhibit good reproducibility with all elements within < 6%RSD. Duplicate measurements of samples 82_HY_06$_a$ and 86_HY_04 showed that the maximum offsets between each pair were less than 5% for all elements, except for Ca (typically > 50%; ESM 1.5).

Control experiments were conducted using sample 82_HY_06$_a$ and synthetic seawater (ASTM D1141-98; ReAgent Chemical Services Ltd) to assess potential dissolution during handling. No mineral dissolution was observed during shaking of the vials. In addition, analyses of the parent leach solutions prior to use showed all elements below < 1 ppm, indicating no contamination from reagents (ESM 1.6).

Statistical methods

Non-linear relationships in elemental data from LA-ICP-MS and SEM-EDS analyses were evaluated using Spearman correlations, median, Mann-Whitney U-tests and element interrelationships in FeOOH tested by t-Distributed Stochastic Neighbour Embedding (t-SNE; Maaten and Hinton 2008) with Kaiser normalisation (Kaiser 1974). The t-SNE method is a dimensionality reduction technique similar to a principal component analysis but designed to be used on non-normally distributed data. The t-SNE tests were conducted in RStudio with data visualisation with the 'ggplot2' package (Wickham 2016), 'dplyr' package for data manipulation (Wickham et al. 2023), 'Rtsne' package to conduct the t-SNE test (Krijthe 2015), 'cluster' for the cluster analysis of t-SNE (Maechler et al. 2023) and 'readxl' package to read Excel files (Wickham and Bryan 2023). Sequential leaching data obtained by ICP-MS and ICP-OES were evaluated by Pearson correlation and described using their means. Full details on statistical methods can be found on ESM 1.2.

Results

FeOOH petrography and mineralogy

Textural morphologies of bulk FeOOH samples obtained from Semenov for this study include chimney, ocherous, and massive types (Fig. 2; Bishop et al. 2025b). Sample 82_HY_06 comprises an FeOOH crust ($82\_HY\_06_a$) mantled over massive sulphide ($82\_HY\_06_b$). Poorly crystalline FeOOH interpreted as ferrihydrite (Jambor and Dutrizac 1998) dominates the samples, comprising over 50 vol%, whereas crystalline FeOOH (goethite) accounts for approximately 8–20 vol%. Minor minerals detected in multiple samples include atacamite (<1 to ~10%) and its polymorph paratacamite (~3–4%), barite (~2–4%), akageneite (~3%), quartz (~1–2%), and calcite (<1 to ~2%; ESM 1.7). Reflective microscopy shows that FeOOH displays a range of mineral morphologies summarised in Fig. 2 with a full description of each morphology in ESM 1.8. Sulphide inclusions within FeOOH were used to determine the FeOOH precursors. For example, FeOOH minerals with pyrite inclusions are classified as pyrite derived FeOOH (py-FeOOH; e.g., Figs. 2H and 3E) and FeOOH with chalcopyrite or covellite inclusions as chalcopyrite derived FeOOH (ccp-FeOOH; Fig. 3D). Both py-FeOOH and ccp-FeOOH are mostly observed in massive sulphide samples and are defined as early formed FeOOH phases that still contain relict sulphide precursor, in contrast to FeOOH with no sulphide. The latter, typically found in fully oxidised samples, likely exhibit advanced oxidation relative to py-FeOOH and ccp-FeOOH and are defined as modified FeOOH. Atacamite occurs as a minor mineral within fully oxidised FeOOH samples and forms as anhedral crystals, vein, or euhedral crystals (Figs. 2E and 3E).

Massive sulphide petrography

Massive sulphide samples are predominantly made of pyrite (>80 vol%), with minor amounts of chalcopyrite, barite, FeOOH, and atacamite (<20 vol%), as well as trace amounts of sphalerite and covellite (Fig. 3). Pyrite displays four textural morphologies: colloform, porous, euhedral, and framboidal (Fig. 3F). Chalcopyrite either forms as inclusions within both euhedral and porous pyrite, or as anhedral grains within texturally massive veins (Fig. 3D). Sphalerite occurs as small inclusions (<10 µm) within euhedral and porous pyrite. Covellite typically forms at the rim or enclosing chalcopyrite (Fig. 3D), indicating its formation through chalcopyrite oxidation.

Geochemical composition of sulphides and their weathering products

Sulphides

Laser ablation ICP-MS was used to assess the major and trace metal composition of different mineral phases. Pyrite is enriched in As, Mo, Au, and Bi, but depleted in Ag relative to other sulphides (Table 1; Fig. 4). Elements of interest in this study in pyrite include Cu (median: 0.36 wt%, max: 5.65 wt%), As (median: 0.40 wt%, max: 2.62 wt%), Zn (median: 0.12 wt%, max: 1.10 wt%), Ag (median: 0.5 ppm, max: 153 ppm) and Au (median: 0.5 ppm, max: 9.4 ppm; Table 1). Ablation depth profiles in pyrite exhibit spikes in Cu, Pb and Zn intensity, suggesting the presence of chalcopyrite, galena, and sphalerite inclusions (Fig. 5). Elevated Ag generally coincides with elevated Au, Cu, or Pb (Figs. 5A-C), with weak positive correlations between Ag and Pb ($R=0.41$) and Au ($R=0.44$) implying Ag is present in electrum, chalcopyrite, or galena inclusions (ESM 3.2). Flat, consistent intensity profiles suggest Au is hosted within the pyrite crystal lattice.

Compared to pyrite, chalcopyrite is enriched in the trace metals Ca, In, and Ag, but depleted in Zn, Co, and As (Table 1; Fig. 4). Statistical U-tests reveal significant differences in Ca, Zn, As, Mo, Sb between chalcopyrite and pyrite (ESM 1.10). Ag in chalcopyrite correlates strongly with Zn ($R=0.82$), Sb ($R=0.80$), Au ($R=0.72$), and In ($R=0.56$), suggesting inclusions of sphalerite, galena, or tetrahedrite (ESM 3.3). Ablation depth profiles (Fig. 5D) show Fe, Ag, Bi, Sb, Au, As, and Pb anomalies, indicating sulfosalt inclusions such as tetrahedrite (Johnson et al. 1986).

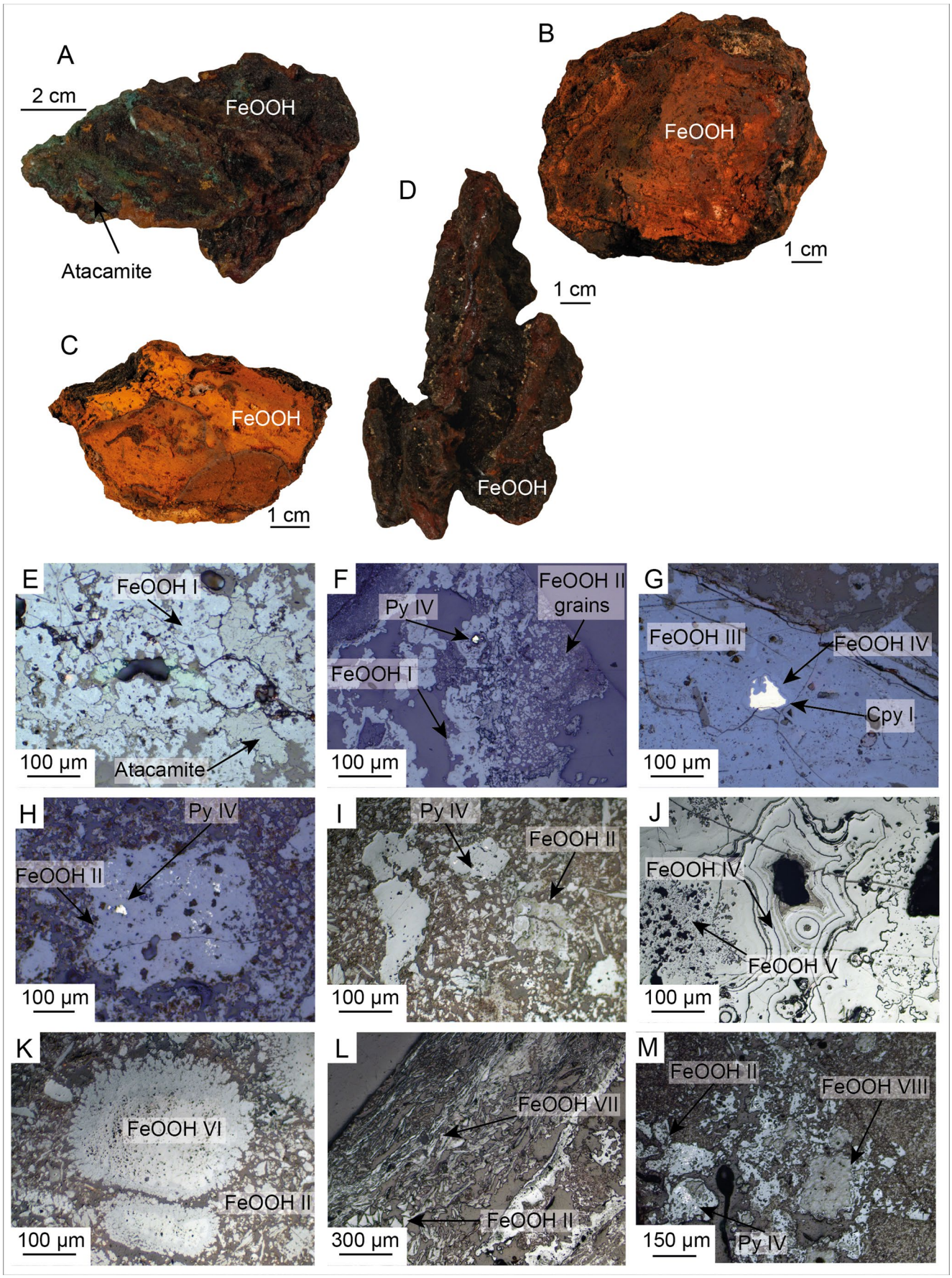
A
2 cm
FeOOH
Atacamite
B
FeOOH
1 cm
C
FeOOH
1 cm
D
1 cm
FeOOH
E
FeOOH I
100 µm
Atacamite
F
Py IV
FeOOH II grains
FeOOH I
100 µm
G
FeOOH III
FeOOH IV
Cpy I
100 µm
H
Py IV
FeOOH II
100 µm
I
Py IV
FeOOH II
100 µm
J
FeOOH IV
FeOOH V
100 µm
K
FeOOH VI
FeOOH II
100 µm
L
FeOOH VII
FeOOH II
300 µm
M
FeOOH II
FeOOH VIII
150 µm
Py IV

Fig. 2 Images and reflected light photomicrographs of FeOOH samples from Semenov. (**A**) 94_HY_06: Reddish-brown FeOOH with a chimney textural morphology from Semenov-4 with Mn-oxide crust and atacamite. (**B**) 87_MC_01: Reddish-brown FeOOH with a massive textural morphology and Mn-oxide crust from Semenov-1. (**C**) 82_HY_05: Ocherous orange-brown FeOOH from Semenov-5. (**D**) 102_HY_04: Dark reddish-brown FeOOH with chimney textural morphology from Semenov-4. (**E**) 102_HY_04: Porous FeOOH I with atacamite. (**F**) 94_HY_06(i): Massive FeOOH I transitioning to FeOOH II grains. Relict pyrite within FeOOH (I) (**G**) 87_MC_01: Relict chalcopyrite (ccp) in colloform FeOOH IV within FeOOH III. (**H**) 94_HY_06(ii): Py-FeOOH grain with pyrite inclusions. (**I**) 82_HY_05: FeOOH II with relict pyrite. (**J**) 82_HY_06$_b$: Dendritic FeOOH V enclosed by FeOOH IV. (**K**) 82_HY_05: Anhedral, porous FeOOH VI with FeOOH (II) (**L**) 82_HY_05: Tabular, euhedral FeOOH VII with FeOOH II grains. (**M**) 82_HY_06$_a$: FeOOH II with pyrite inclusions overlain by FeOOH VIII. Panels A, C, D and I are modified from Bishop et al. (2025a)

FeOOH and atacamite

Typically, Py-FeOOH, is enriched in Si, Cu, Zn, As, Mo, In, Sb, REE and Au compared to pyrite across the dataset, but depleted in Co, Ag and Bi (Table 1). Relative to chalcopyrite, ccp-FeOOH, is enriched in most elements except for Cu (Table 1). A U-test reveals significant Si, Ca, Fe, Co, Ni, As, and Ag differences between py-FeOOH ($n=6$) and ccp-FeOOH ($n=9$; ESM 1.10). Correlations in py-FeOOH and ccp-FeOOH include Cu-Ag ($R=0.54$) and inverse Cu-Zn (-0.69), whereas Zn positively correlates with In (0.85) and Bi (0.57) but negatively with Na (-0.55) and Ca (-0.62; ESM 3.5). Depth profiles of ccp-FeOOH show Cu spikes correlate with Ag, suggesting relict Cu-sulphide inclusions (7/9 spots; Fig. 5E). Some py-FeOOH profiles show Au and Ag concentrations together (e.g., 06iiS5-2), while others show opposing trends (e.g., 06iiS7-1) or spikes of Au alone (e.g., 06iiS5-6), indicating Au and Ag are not always co-enriched.

The median Cu content of modified FeOOH is 2.86 wt% (Fig. 4C) and correlates positively with Pb ($R=0.53$), S (0.45), and In (0.42), but negatively with Na (-0.56). Zinc is uncorrelated to other elements. Modified FeOOH are depleted in Au and Ag (median concentration of <0.1 ppm) compared to sulphides and py-FeOOH/ccp-FeOOH (Fig. 4E and F; Table 1). Calcium correlates with Na (0.68) and Si (0.80) and inversely with Sb (-0.76), Mo (-0.71), As (-0.59), and Au (-0.44; ESM 3.4). Generally smooth ablation profiles for Si, Ca, Cu, Zn, Mo, As and Sb in 168/230 spots indicate lattice substitution or even distribution of adsorbed metals (Fig. 5F; ESM 4). Compared to modified FeOOH, both py-FeOOH and ccp-FeOOH are depleted in Si, Cl, Ca, Mn and REE but enriched in Cu, Mo, Ag, Au and Bi. Statistical U-tests show significant differences in most elements except Mg, Fe, and Ce (ESM 1.10).

Atacamite is depleted in concentrations of most trace metals relative to FeOOH and chalcopyrite (Table 1). Ablation depth profiles of most elements (e.g., As, Au, Ag, La, Sb, Mo) correlate with spikes and jumps of Fe suggesting the presence of FeOOH or possibly Fe-sulphides (e.g., 01S5-7 and 06FS5-9; ESM 4).

REE concentrations

Rare earth element (REE) concentrations, and particularly the presence of negative Ce anomalies, can help to trace interactions of minerals with seawater during seafloor weathering (De Baar et al. 1985). While FeOOH and atacamite are expected to exhibit a partly seawater-like REE signature (Dekov et al. 2011; Maslennikov et al. 2023), they may also retain the signature of the sulphide precursor (ESM 3.6).

Fe-oxyhydroxide are enriched in the sum of rare earth element concentrations (ΣREE) compared to pyrite and chalcopyrite by approximately one or two orders of magnitude, respectively (Fig. 4D), and have a negative Ce anomaly (median of -0.55; Table 1). The REE content in FeOOH has a weak negative correlation with In (R = -0.49), Sb (-0.36), S (-0.52) and weak positive correlation with Ca (0.50), Ni (0.43) and Si (0.41; ESM 3.4). Early formed Py-FeOOH and ccp-FeOOH are depleted in ΣREE relative to modified FeOOH but enriched in LREE compared to their respective sulphide precursor (Fig. 4D). Atacamite is depleted in REE elements relative to FeOOH and chalcopyrite and exhibits negative Ce anomalies with a median of 0.67.

Geochemical data by SEM-EDS

Sample 82_HY_06 (Fig. 3) allows for direct comparison of precursor massive sulphide (82_HY_06$_b$) with early formed ccp-FeOOH, py-FeOOH and modified FeOOH from the oxidised crust (82_HY_06$_a$). Since 82_HY_06$_b$ contains FeOOH too small for LA-ICP-MS, SEM-EDS measurements are used (ESM 3.7). Modified FeOOH (82_HY_06$_a$) is enriched in Si, Cu, Cl, and Ca but depleted in S, Fe, and Zn compared to FeOOH in 82_HY_06$_b$ (Table 2). A statistical U-test confirms significant differences in S, Si, Fe, Cu, Zn, Cl, and Ca composition between modified FeOOH in 82_HY_06$_a$ and unmodified FeOOH in 82_HY_06$_b$ (ESM 1.10). Spearman's correlations show Cu negatively correlates with S (-0.43), Fe (-0.71), and Zn (-0.48), but positively with Si (0.40), Cl (0.46), and Ca (0.50; ESM 3.8).

Elemental mapping of active sulphide weathering sites

To assess trace element mobility during the conversion from sulphide to FeOOH, LA-TOF-ICP-MS elemental mapping was performed on sample 82_HY_06$_b$ (Fig. 6). At the first site, pyrite oxidation at a redox front is marked

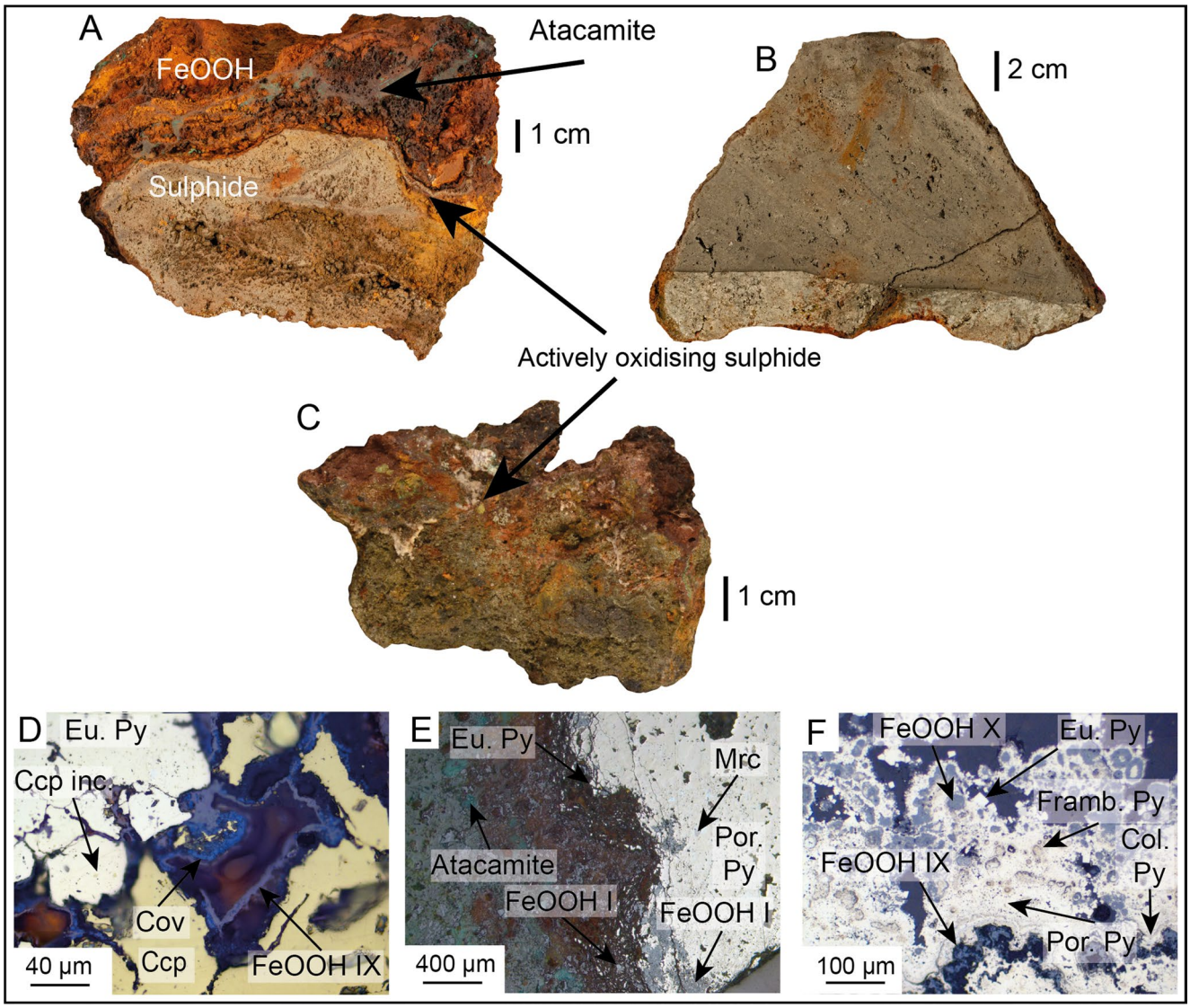

Fig. 3 Representative images and reflective light photomicrographs of sulphide samples from the Semenov hydrothermal cluster. (**A**) 82_HY_06: Comprises of an FeOOH crust with a massive textural morphology and atacamite veins (82_HY_06$_b$) overlying massive sulphide (82_HY_06$_a$) from Semenov-5. (**B**) 86_HY_07: Pyrite-dominated massive sulphide from Semenov-4. (**C**) 90_HY_04: Barite-rich massive sulphide with weathered Fe-oxide coatings from Semenov-4. (**D**) 82_HY_06$_a$: Euhedral pyrite with chalcopyrite inclusions, anhedral, corroded chalcopyrite, and secondary covellite; FeOOH X linked to chalcopyrite alteration. (**E**) 82_HY_06$_a$: Porous and euhedral pyrite, replaced by FeOOH I and brecciated, with atacamite in oxidised areas. (**F**) 90_HY_04: Multiple pyrite morphologies (euhedral, framboidal, porous, colloform) with FeOOH X replacing framboidal pyrite, alongside bluish-grey FeOOH IX. Panels A, D and E are modified from Bishop et al. (2025a)

by brecciation of the pyrite and replacement by FeOOH (Fig. 6A). Where py-FeOOH is observed within pyrite, py-FeOOH is enriched in Cd and Cu, but depleted in Ag relative to pyrite. Gold and Ag exhibit concomitant enrichment at the redox front, particularly on pyrite rims, but are depleted in FeOOH (Fig. 6D).

At the second site, chalcopyrite oxidation leads to its replacement by covellite and FeOOH (Fig. 6G). Covellite shows the highest enrichment in Cu, Au, and Ag among all the sulphides studied, while sphalerite is most enriched in Cd. Chalcopyrite derived FeOOH forms as pseudomorphs of chalcopyrite and is enriched in Cd but depleted in Cu, Ag, and Au relative to its chalcopyrite protolith. Au and Ag are typically concentrated along chalcopyrite rims and in covellite.

Sequential leaching experiments

Sequential leaching studies with bulk samples of FeOOH isolate the compositions of atacamite (leach 2), ferrihydrite

Table 1 Median values of trace elemental data of sulphide minerals, FeOOH and atacamite. [a] Elements obtained by quantitative SEM-EDS. Values obtained for modified FeOOH exclude py-FeOOH and ccp-FeOOH. The Ce and Eu anomalies (Ce* and Eu*) are calculated as a geometric mean interpolation after McLennan (1989) using the following formula $Ce^* = Ce_N/(La_N \times Pr_N) \times 0.5$ and $Eu^* = Eu_N/(Sm_N \times Gd_N) \times 0.5$. Normalised values ($X_N$) obtained from chondrite values after Sun and McDonough (1989) Note, Ce and Eu anomalies were compiled using data above limit of detection. See ESM 3.6 for full details. < LOD – below detection limit

	Primary sulphides		Weathering products			
	Pyrite ($n=43$)	Chalcopyrite ($n=18$)	Py FeOOH ($n=6$)	Ccp FeOOH ($n=9$)	Modified FeOOH ($n=215$)	Atacamite ($n=30$)
Na[a] (wt%)	< LOD	< LOD	0.16	0.26	0.43	< LOD
Mg[a] (wt%)	< LOD	< LOD	0.3	0.34	0.32	< LOD
Si (wt%)	<0.1	<0.1	1.9	1.5	3.1	< LOD
S[a] (wt%)	53.15	34.45	0.15	0.47	0.15	< LOD
Cl[a] (wt%)	< LOD	< LOD	0.26	0.19	0.35	15.64
Ca (wt%)	0.17	0.30	0.14	0.31	0.40	0.01
Fe (wt%)	46.55	30.78	49.63	45.52	47.55	0.72
Cu (wt%)	0.36	31.20	3.10	4.36	2.84	57.36
Zn (wt%)	0.12	0.02	0.20	0.18	0.12	0.02
Al (ppm)	900	1550	1000	3100	400	50
Mn (ppm)	5	2	6	3	20	<1
Co (ppm)	41	9	7	35	2	3
Ni (ppm)	1	<1	9	2	5	<1
As (ppm)	404	8	976	28	174	11
Mo (ppm)	60	43	346	495	173	40
Ag (ppm)	4.9	18.5	0.2	25.5	<0.1	<0.1
In (ppm)	1.6	6.7	11.4	9.7	0.1	<0.1
Sb (ppm)	9	2	36	23	8	<1
Au (ppm)	0.5	<0.1	1.3	0.3	<0.1	<0.1
Pb (ppm)	81	26	85	144	26	<1
Bi (ppm)	4.8	0.8	1.0	7.8	<0.1	5
ΣREE (ppm)	0.1	0.2	1.7	0.7	5.8	0.1
Ce*	0.64	0.85	0.82	0.46	0.41	0.67
Eu*	0.88	N/A	0.86	1.37	0.77	0.80

(leach 3), and goethite (leach 4) to understand metal distribution among these phases and their influence on FeOOH composition. Leach 1 removes sorbed metals, with >99% of Cu, Zn, and Fe not sorbed (Fig. 7). Leach 2 effectively extracts atacamite, indicated by low Fe recovery (0.5% of total Fe) and high Cu recovery (42.6%). Leach 3 targets ferrihydrite and reducible FeOOH phases, extracting ~63% of Fe and ~38% of Cu. Leach 4 attacks crystalline FeOOH such as goethite, extracting ~12% of Fe and ~6% of Cu (Fig. 7, ESM 1.11). Leach 2 recovers the most Cu (~2.9 wt%), followed by leach 3 (~1.4 wt%; Fig. 7B). Bulk Cu content strongly correlates with Cu dissolved in leach 2 ($R^2 = 0.99$) and leach 3 ($R^2 = 0.77$) but not leach 4 ($R^2 = 0.23$). Leach 3 extracts the most Fe (~30 wt%), followed by leach 4 (~5.8 wt%). Zn is primarily extracted in leach 3 (~57%) and leach 4 (20%).

t-SNE analysis

To test elemental interrelationships and identify potential sources modifying FeOOH composition, a t-SNE analysis was performed on FeOOH using the quantitative LA-ICP-MS spot data. K-means clustering of the t-SNE results produced five clusters (Fig. 8), with each forming a distinct grouping, although clusters 3 and 4 partially overlap.

Cluster 1 comprises Mo–As–In–Sb–Pb–Al, while Cluster 2 contains Ca–Na–Si–Mg–Fe. Cluster 3 groups Cu–S–Cl, Cluster 4 is characterised by Ni and REE, and Cluster 5 by Mn and Co. Because t-SNE is a non-linear dimensionality-reduction method, the absolute distances and axes in the plot have no quantitative meaning; however, the method reliably identifies local neighbourhood structure, and the clusters represent distinct elemental associations within the FeOOH composition.

Discussion

Origin of Fe-oxyhydroxide at Semenov

Previous work after Bishop et al. (2025a) interpreted the samples of FeOOH in this study as secondary FeOOH (i.e., products of sulphide weathering). Petrographic results here show sulphide grains enclosed within FeOOH (e.g. FeOOH I: Fig. 2F; FeOOH II: Fig. 2H; FeOOH IV: Fig. 2G) and FeOOH forming as psuedomorphs after pyrite (e.g. FeOOH

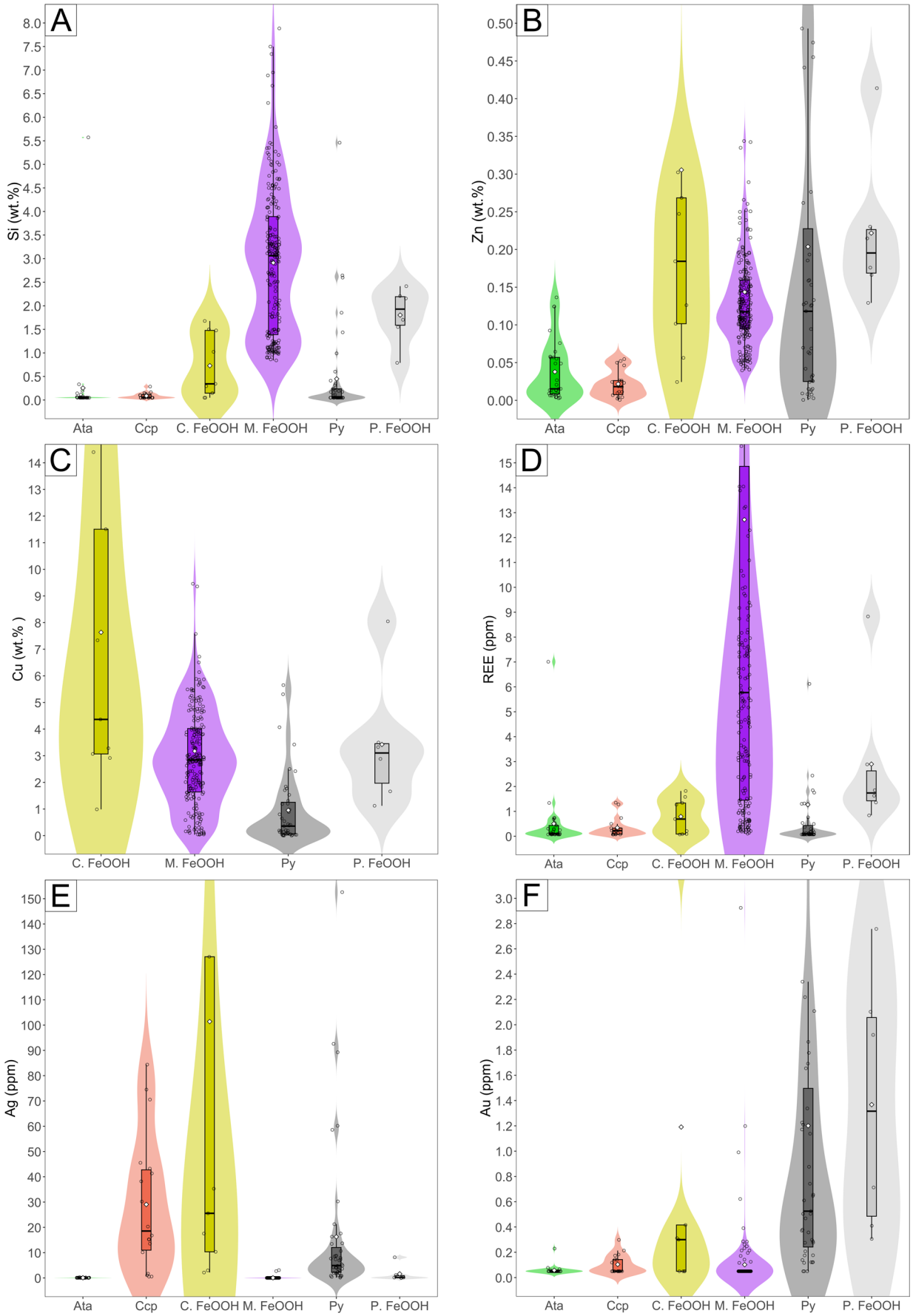
A
Si (wt.%)
Ata
Ccp
C. FeOOH
M. FeOOH
Py
P. FeOOH
B
Zn (wt.%)
C
Cu (wt.%)
D
REE (ppm)
E
Ag (ppm)
F
Au (ppm)

Fig. 4 Combined box and violin plots showing the distribution of element concentrations in sulphide minerals and their weathering products for (**A**) Si (wt%), (**B**) Zn (wt%), (**C**) Cu (wt%), (**D**) REE (ppm), (**E**) Ag (ppm) and (**F**) Au (ppm). The width of the violin reflects the frequency of values at a given concentration. Lower and upper fences are the 25th and 75th percentiles, the horizontal black bar in the box represents the median, the white diamond in the box is the average and the whiskers beyond the box plot represent the 10th and 90th percentiles. Individual data points are shown as dots. The horizontal black bar represents the median, and the white dot within the plot shows the mean. Abbreviations: Ccp – chalcopyrite, Ata – atacamite, Py – pyrite, C. FeOOH – chalcopyrite-derived FeOOH, P. FeOOH – pyrite-derived FeOOH

I: Fig. 3E), suggest that instances of FeOOH I, FeOOH II and FeOOH IV are secondary FeOOH. Positive Eu anomalies have been reported in some primary hydrothermal Fe–Si precipitates (Mills and Elderfield 1995; Dong et al. 2022; Gini et al. 2024). However, other studies document primary FeOOH without a Eu anomaly (Hekinian et al. 1993), and secondary FeOOH formed during sulphide oxidation can also display positive Eu anomalies (Hu et al. 2022). The FeOOH analysed in this study shows flat to negative Eu anomalies. Taken together, these observations demonstrate that Eu behaviour varies widely in both primary and secondary FeOOH, which limits the usefulness of Eu/Eu* or REE patterns as indicators of formation environment. Instead, the Si–Fe–(Zn + Cu + Co + Ni)×10 ternary classification of Hekinian et al. (1993) is more reliable here: the vast majority of our analyses plot as Type 2 (consistent with secondary FeOOH; ESM 1.12). Across all samples, 198 of 215 measurements classify as secondary; exceptions include 87_MC_01 (8/28 Type 1) and 102_HY_04 (9/46 Type 1), where these phases are more likely primary precipitates. Together, textures, sulphide relationships, and bulk-chemistry fields indicate that the FeOOH measured from this study are predominantly secondary FeOOH.

The mobility and behaviour of metals during sulphide weathering

Understanding the behaviour of economic metals (e.g., Cu, Zn, Au and Ag) during seafloor weathering is critical to assess whether ageing SMS deposits preserve their economic potential. At Semenov, the FeOOH derived from the oxidation of pyrite and chalcopyrite initially reflect compositional inheritance from the sulphide precursor, i.e., py-FeOOH are enriched in As, Fe, Au and depleted in Ca, Cu and Ag relative to ccp-FeOOH (ESM 1.9). However, metal concentrations in FeOOH often deviate from mass balance expectations. For example, consider pyrite that contains a median concentration of 0.36 wt% Cu that transforms to py-FeOOH. During this transformation, approximately 26% of the original mineral mass is lost. In the absence of Cu mobilisation, this mass loss alone should concentrate the Cu to ~0.5 wt%. However, 3.1 wt% Cu is observed, indicating that additional Cu is captured from external sources. Moreover, metals such as Zn, Mo and Sb show similar concentrations in both py-FeOOH and ccp-FeOOH, irrespective of the concentration of these metals in the sulphide precursor and thus, their concentrations are not inherited solely from the precursor and may be modified during or post-formation. The FeOOH identified in this study include early formed, minimally modified py-FeOOH and ccp-FeOOH, with visible relict sulphide or visible sulphide association, and modified FeOOH without relict sulphide or their association in fully oxidised bulk samples (Fig. 2). Relative to both py-FeOOH and ccp-FeOOH, modified FeOOH are significantly enriched in elements such as Si, Cl, Ca and REE, and depleted in Cu, Zn, Mo, Ag, Sb and Au, indicating a compositional evolution of FeOOH (Hu et al. 2022).

The t-SNE clustering results support this interpretation of FeOOH compositional evolution. Cluster 1 is characterised by Mo–As–In–Sb–Pb–Al associations. Arsenic, In, Sb, and Pb are consistent with inheritance from sulphide phases (Maslennikov et al. 2023). Aluminium concentrations are lower in FeOOH relative to the sulphide phases and show no correlation with clay tracers (e.g., Si, Mg, Na, Ca), which suggests that Al is largely inherited from the sulphide rather than derived from detrital aluminosilicates. Molybdenum is enriched in FeOOH relative to primary sulphides and may reflect seawater Mo scavenged in locally acidic and reducing microenvironments at the sulphide–seawater reaction front (thiomolybdate pathways; Erickson and Helz 2000; Maslennikov et al. 2023). Under oxic, circumneutral conditions, however, molybdate is relatively unreactive and only weakly adsorbed to FeOOH, preventing progressive Mo enrichment during continued seawater overprint (Erickson and Helz 2000; Brinza et al. 2019). Together, these features indicate that Cluster 1 reflects trace element incorporation during sulphide oxidation under seawater influence.

Cluster 2 is characterised by Ca-Na-Mg-Si-Fe. The association of Ca, Na and Mg indicates strong seawater influence (Mendez and Hiemstra 2020; Maslennikov et al. 2023), Fe is sourced from the oxidation of sulphide precursors rather than directly from seawater. Silicon does not correlate with Al (ESM 3.4) that would indicate smectite inclusions, and LA-ICP-MS depth profiles do not display concurrent Al spikes, suggesting that detrital clays are not the dominant source of Si. Silicon can be incorporated at the time of ferrihydrite precipitation (Parfitt et al. 1992; Hu et al. 2023) or alternatively can sorb onto FeOOH surfaces (Davis et al. 2002; Swedlund et al. 2011; Sugiyama and Halevy 2024). Therefore Cluster 2 most likely records progressive seawater overprint of FeOOH, in which dissolved silica and major seawater cations are taken up by or exchanged with FeOOH surfaces during continued exposure to seawater.

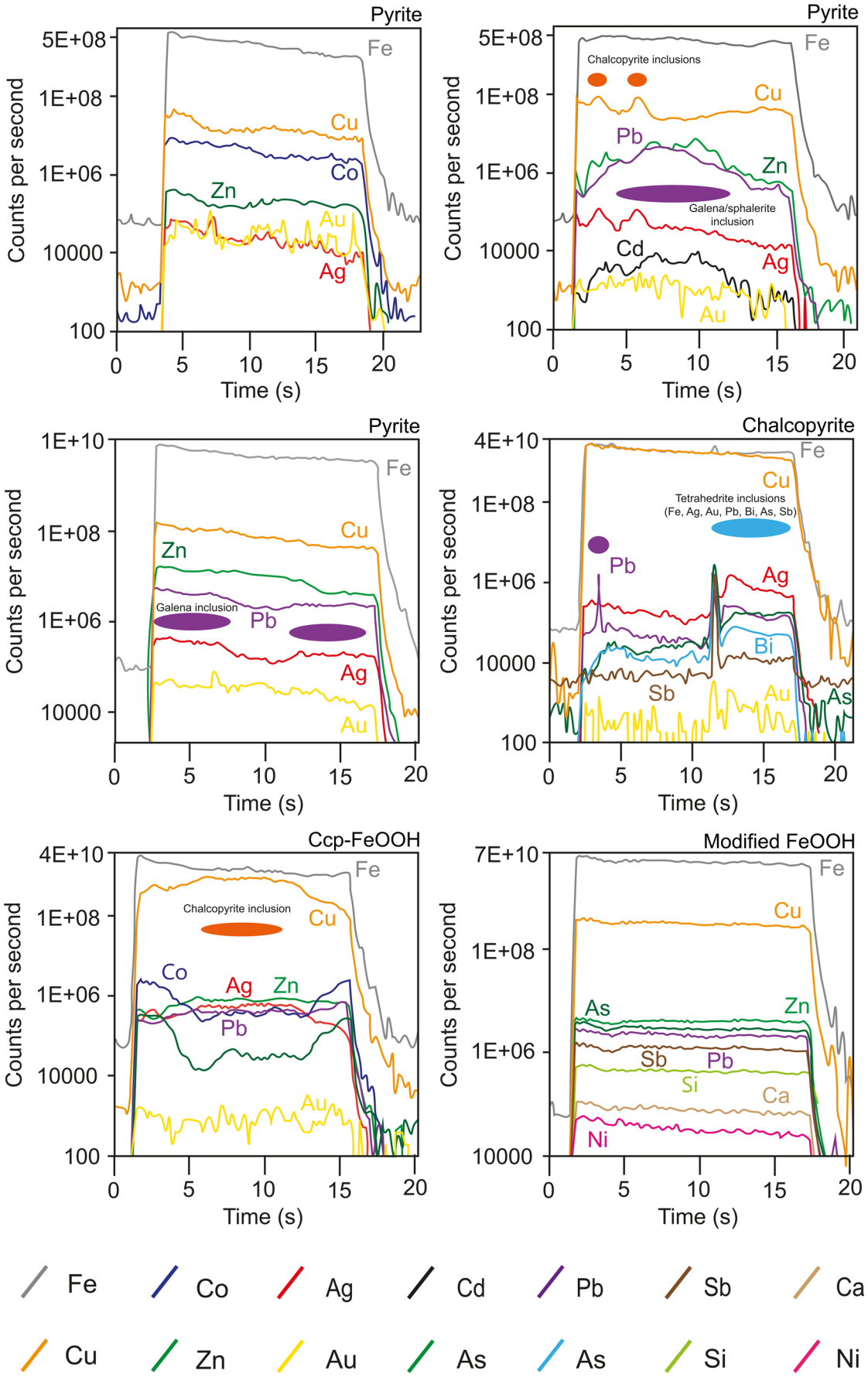
Pyrite
Counts per second
Time (s)
Fe
Cu
Co
Zn
Au
Ag
Pyrite
Chalcopyrite inclusions
Galena/sphalerite inclusion
Pb
Cd
Pyrite
Galena inclusion
Chalcopyrite
Tetrahedrite inclusions
(Fe, Ag, Au, Pb, Bi, As, Sb)
Bi
Sb
As
Ccp-FeOOH
Chalcopyrite inclusion
Modified FeOOH
Si
Ca
Ni

Fig. 5 LA-ICP-MS ablation depth profiles for sulphides and FeOOH. (**A**) Porous pyrite (07S4-4, 86_HY_07): Smooth Co and Fe traces; jumps in concentration of Cu and Zn indicate chalcopyrite and sphalerite inclusions, while Au and Ag spikes suggest electrum OR native Au. (**B**) Euhedral pyrite (07S7-3, 86_HY_07): Pb-bearing sphalerite or galena inclusions, with chalcopyrite and Ag spikes; Au trace suggests lattice substitution in pyrite. (**C**) Euhedral pyrite (06S6-5, 82_HY_06): Galena inclusions correlate with Ag spikes; stable Au, Zn, and Cu suggest solid substitution in pyrite. (**D**) Anhedral chalcopyrite (06S12-4, 82_HY_06): Galena and tetrahedrite inclusions with As, Au, Sb, Bi, Pb, Ag, and Fe spikes. (**E**) Ccp-FeOOH (07S6-1, 86_HY_07): Large Cu sulphide inclusion with correlating Ag. (**F**) Modified FeOOH (05S2-2, 82_HY_05): Smooth elemental profiles, indicating solid substitution or even adsorption of Fe, Cu, Zn, As, Sb, Pb, Si, Ca, and Ni in FeOOH

The Cu–S–Cl association in Cluster 3 suggests a pathway involving seawater oxidation of Cu-sulphides. The oxidation of Cu-sulphides may mobilise Cu as Cu-Cl chloro-complexes (Rose 1976; Hannington 1993) that can subsequently adsorb onto FeOOH (Moon and Peacock 2012; Chesne and Kim 2014), while co-released sulphur is oxidised to sulphate (Dileep Kumar 1981) that also readily sorbs onto FeOOH (Namayandeh et al. 2022). Clusters 4 and 5 may result from hydrothermal fluid-seawater mixing (e.g., Roy 1992), precipitating Mn-oxides, or through hydrogenous Mn-oxide precipitation that associate with Co and Mn in cluster 5, and Ni and REE in cluster 4 (Elderfield et al. 1981). Though similar in origin, cluster 5 may also stem from other processes, such as seawater (REE-Ni) interaction with FeOOH or sulphide oxidation (Zn; Maslennikov et al. 2023). Together, these clusters illustrate the various inputs to the geochemical composition of FeOOH, from sulphide-derived elements to seawater-derived compositions.

In summary, while the sulphide precursor mineral initially influences FeOOH composition (e.g., Cu, As, Au, Ag), external inputs also control modified FeOOH composition (e.g., Ca, Cu, Si, REE). Without knowing the protolith of modified FeOOH, it is challenging to trace the geochemical evolution of FeOOH and thus, assess its role as a metal trap and a potential additional resource in SMS deposits.

The evolution of FeOOH composition

Identifying the sulphide protolith

To trace the sulphide protolith and the geochemical evolution of modified FeOOH, two ternary diagrams were constructed using LA-ICP-MS data (Fig. 9A and B). Both py-FeOOH and ccp-FeOOH closely associate with their protolith (Fig. 9A), with most FeOOH derived from pyrite, reflecting its dominance in the system (Maslennikov et al. 2023; Fig. 9C). The majority of modified FeOOH plot between pyrite and chalcopyrite end-members (Fig. 9A), suggesting a mixed sulphide composition. Furthermore, outliers of py-FeOOH and ccp-FeOOH also fall into this mixed composition field (Fig. 9A) that display similar morphologies with modified FeOOH (Figs. 2 and 3), implying that their hybrid signature arose through post-formational modification (e.g., sulphide oxidation). Data reduction t-SNE analysis of FeOOH indicates that post-formational modification sources include seawater interaction (Mg-Ca-Na-Si), elements derived from sulphide oxidation (i.e., Cu-S-Zn) and precipitation of Mn-oxides (i.e., Co-Mn). This is further supported by SEM-EDS of 82_HY_06, showing that relative to py- and ccp-FeOOH, modified FeOOH are enriched in Cu and seawater elements (i.e., Ca-Si-Mg), but depleted in other sulphide derived elements (e.g., S and Zn). Seawater interaction is further evidenced by modified FeOOH showing an increased negative Ce anomaly relative to py-FeOOH and ccp-FeOOH. Progressive seawater modification can be observed on Fig. 9B and D whereby minimally modified FeOOH occupy areas of low seawater influence (high As/Ca, Fe/Cu and low Si/Mo), while modified FeOOH trend towards high seawater modification (i.e., high Si/Mo, low As/Ca and Fe/Cu).

These findings suggest FeOOH inherits its initial composition from the protolith, but undergoes post-formational modification, becoming enriched in Na, Mg, Ca, Cl, Si, REEs, and Cu while progressively depleted in Zn, Sb, Mo, and As and obscuring the original geochemical inheritance from the sulphide protolith. At this stage it is unclear if the lower content of trace metals of the hydrothermal samples carrying the strongest seawater signature relates to an effective loss of Zn, Sb, Mo and As to an open system, or a dilution of the geochemical content of the sulphide weathering product by addition of seawater-derived elements. As geochemical analysis is weight-normalised, both options are consistent with the data. Unfortunately, an isocon analysis (Gresens 1967; Grant 1986) could not be conducted due to a lack of clear relationship between samples' stages of alteration successions. However, seawater addition alone cannot explain the observed enrichment of Cu in FeOOH. The t-SNE analysis reveals a Cu-Cl-S association, potentially linked to chalcopyrite oxidation or atacamite precipitation, which may account for the observed Cu enrichment.

The influence of atacamite on the composition of FeOOH

The Cu extracted from ferrihydrite in the leaching experiment has a moderate positive correlation with the quantity of (par)atacamite in the sample ($R^2 = 0.52$; Fig. 10A) and

Table 2 Summary major geochemical data of FeOOH obtained from 82_HY_06$_a$ and 82_HY_06$_b$ by SEM-EDS showing median concentration. The first number of sample size for each element (n = X, X) is the measurement number for 82_HY_06$_a$ with the latter number the number of measurements for 82_HY_06$_b$

	S (wt%) n = 73, 174	Si (wt%) n = 74, 174	Fe (wt%) n = 74, 174	Cu (wt%) n = 74, 172	Zn (wt%) n = 3, 119	Cl (wt%) n = 74, 167	Ca (wt%) n = 74, 73
82_HY_06$_a$(modified FeOOH)	0.29	1.82	46.63	4.78	0.28	0.78	0.24
82_HY_06$_b$ (recent FeOOH)	0.58	1.74	49.51	2.52	0.86	0.21	0.10

the Cu extracted from (par)atacamite (R^2 = 0.69; Fig. 10B). This correlation suggests that Cu-rich conditions promote both higher Cu uptake in ferrihydrite and greater (par)atacamite abundance. However, this may also reflect (par)atacamite dissolution during leach 2, followed by adsorption of Cu onto ferrihydrite and subsequent release during leach 3 (e.g., Moon and Peacock 2012), which could underestimate the Cu in (par)atacamite and overestimate it for ferrihydrite. Regardless, these observations highlight the capacity of FeOOH to adsorb Cu from low-pH solutions (e.g., pH 4.5 in leach 2), similar to processes occurring during weathering of SMS deposits. For instance, during chalcopyrite oxidation, Fe precipitates as FeOOH (Glasby and Schulz 1999) whereas Cu is mobilised in chloride complexes (Rose 1976; Hannington 1993). At low pH (e.g., 4.5), (par)atacamite may precipitate (Sharkey and Lewin 1971); however, Cu likely migrates in solution through the FeOOH and then reprecipitate as (par)atacamite upon interaction with seawater (Hannington 1993). As such, the Cu will instead adsorb onto FeOOH, enriching it in Cu as well as Cl. This is supported by t-SNE (Cu–Cl–S) analysis and by the higher Cu and Cl contents in modified FeOOH (82_HY_06$_a$) relative to minimally modified FeOOH (82_HY_06$_b$). Eventually, when cuprous chloride complexes mix with seawater, buffering pH, Eh, and Cl^- activity, (par)atacamite precipitates in voids within FeOOH crust veins (Fig. 3A) or on surfaces directly exposed to seawater (Fig. 2A; Woods and Garrels 1986; Pollard et al. 1989; Hannington 1993).

These observations highlight the role of FeOOH as a metal trap, retaining Cu that might otherwise be lost to seawater. For seafloor exploration, atacamite occurrences likely mark zones where FeOOH crusts are enriched in Cu, and they may also point to underlying Cu-rich sulphide mineralisation. By contrast to ferrihydrite, goethite hosts only ~ 2.5% of the total Cu (0.11 wt%) in the bulk FeOOH samples and shows no correlation with atacamite (Fig. 10). This contrasts with ferrihydrite, where samples containing abundant atacamite are associated with higher Cu concentrations, suggesting that Cu enrichment is primarily associated with ferrihydrite rather than goethite. As goethite forms through the crystallisation of ferrihydrite, this transformation may lead to Cu and Zn loss to seawater during crystallisation, thereby reducing the metal tenor of FeOOH at SMS deposits (Grundl and Delwiche 1993; Blowes et al. 2003; Vu et al. 2013; Sajih et al. 2014).

The crystallisation of ferrihydrite

Sequential leaching studies show that if ferrihydrite fully crystallises into goethite, the Cu content in FeOOH drops from 1.4 wt% to 0.11 wt% (92% loss), and the Zn content decreases from 0.09 wt% to 0.03 wt% (57% loss; Fig. 7). As such, it would be expected that an increasing proportion of goethite would correlate with Cu and Zn depletion. However, correlations between goethite percentage and metal content in the total FeOOH fraction (leaches 3 and 4) yield statistically weak relationships, with R^2 values of 0.11 for Cu (Fig. 10D) and 0.14 for Zn. These low correlation coefficients indicate that the proportion of goethite does not reflect the Cu or Zn content within the FeOOH. Within natural systems, at an SMS deposit, the metals released during goethite crystallisation may re-adsorb onto adjacent FeOOH phases, thereby limiting net metal loss from the system despite increasing goethite formation (Vu et al. 2013). However, since goethite has lower metal adsorption capacity than ferrihydrite, extensive goethite crystallisation could exceed the system's ability to retain released Cu and Zn, ultimately leading to metal depletion (Sajih et al. 2014; Görn et al. 2021). The extent of metal loss would therefore depend on the crystallisation rate of goethite, available adsorption sites, and local geochemical conditions. While outside the scope of this study, the rate of goethite crystallisation is influenced by the adsorption of Fe^{2+}, competition with adsorbed or lattice-bound metals (e.g., Cu, Zn, As; Tronc et al. 1992; Jambor and Dutrizac 1998), and bacterial interactions (Kennedy et al. 2004).

In summary, although ferrihydrite-to-goethite crystallisation has the potential to drive substantial Cu and Zn loss, the weak correlations observed here indicate that goethite abundance alone does not control metal depletion; instead, net metal retention is likely buffered by re-adsorption onto FeOOH and constrained by adsorption capacity and local geochemical conditions.

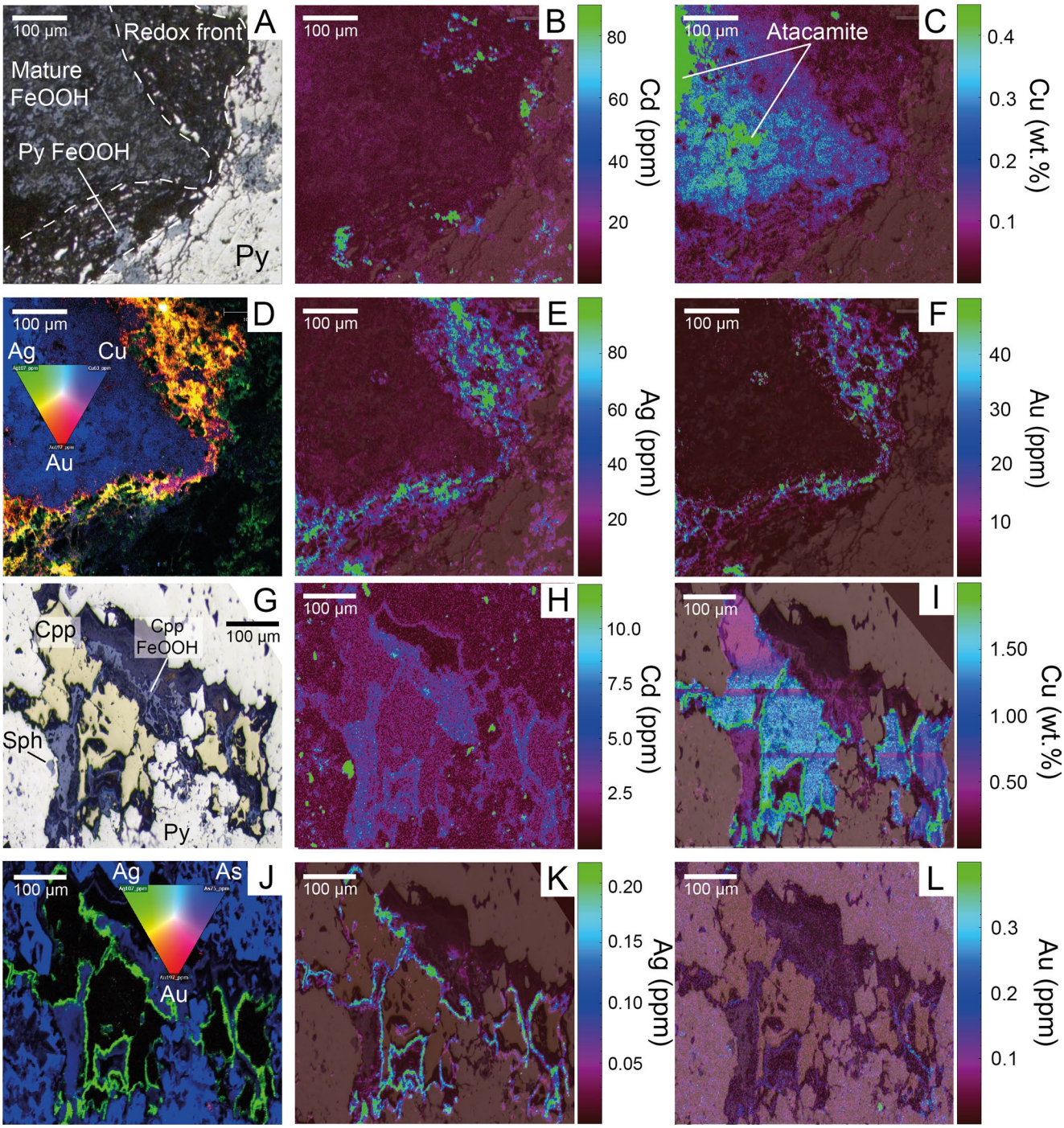

Fig. 6 Semi-quantitative LA–TOF–ICP–MS trace elemental maps for two sites of actively weathering sulphide within 82_HY_06$_b$. (**A**) Reflective microphotograph image of site 1 and trace elemental maps for (**B**) Cd, (**C**) Cu, (**E**) Ag and (**F**) Au. (**D**) shows a red-green-blue image for Au, Ag and Cu respectively to illustrate their correlation. (**G**) Reflective microphotograph image of site 2 with element maps of (**H**) Cd, (**I**) Cu, (**K**) Ag and (**L**) Au. (**J**) illustrates a red-green-blue image for Au, Ag and As respectively to show their correlation. Ccp – chalcopyrite, py – pyrite, sp - sphalerite

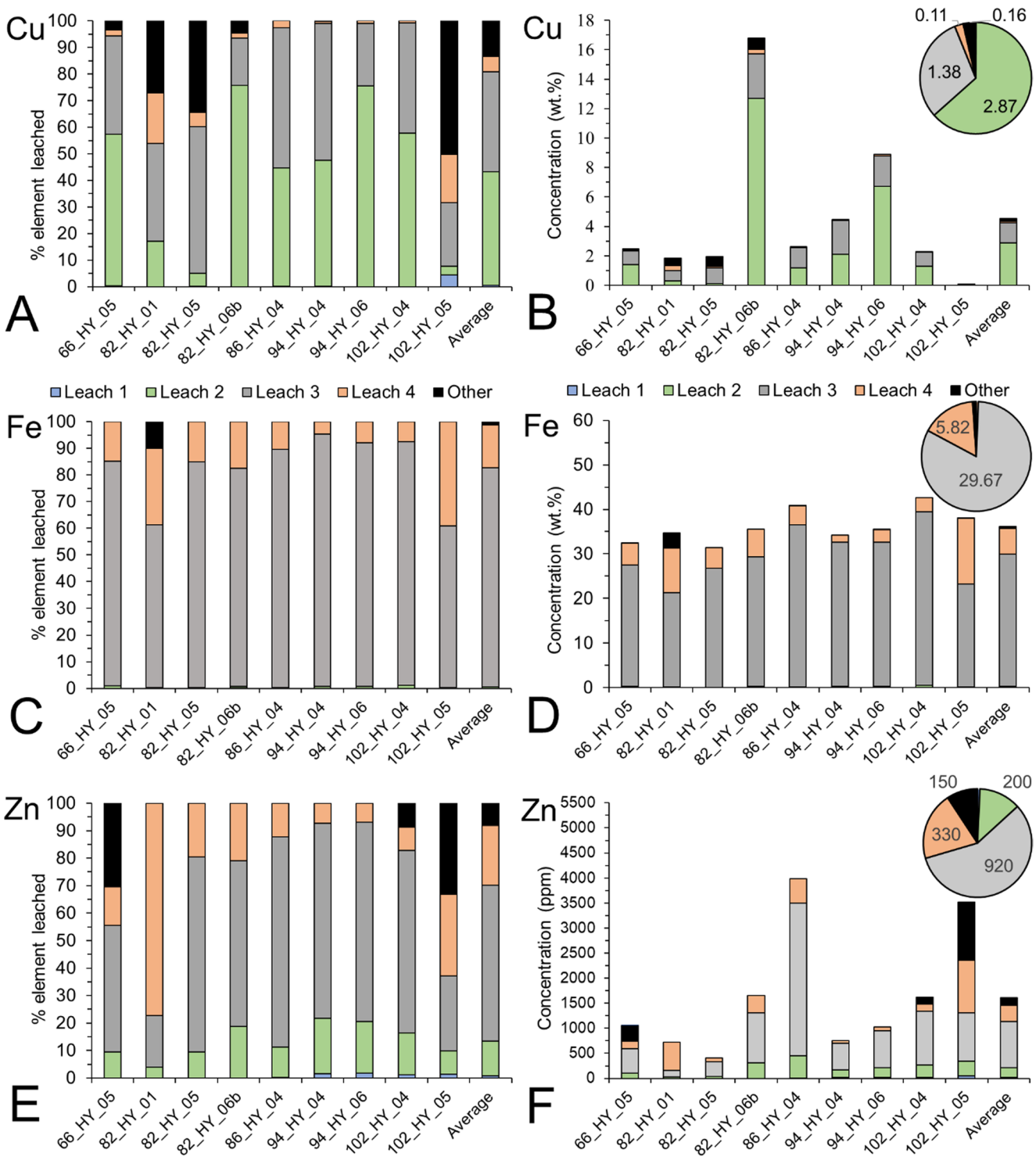

Fig. 7 Percentage element leached and concentration of Cu **(A**, **B)**, Fe **(C**, **D)** and Zn **(E**, **F)** in the leaches of the nine samples of secondary FeOOH from Semenov with the average. The pie chart in the total concentration depicts the average concentration of the nine samples. Leach 1 extracts adsorbed metals. Leach 2 dissolved carbonates and atacamite. Leach 3 extracts easily reducible Fe-oxide and FeOOH such as ferrihydrite. Leach 4 targets crystalline phases of Fe-oxides and FeOOH such as goethite. Note, for average calculation, outliers are removed

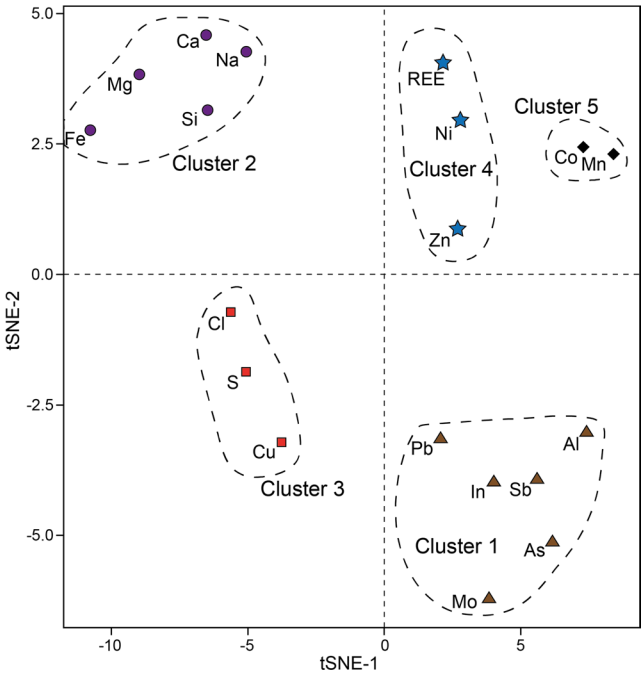

Fig. 8 t-SNE and k-means clustering analysis on modified FeOOH measurements (n=205). Five clusters are compiled including; (1) Cu-S-Cl, (2) Mo-As-In-Pb-Sb-Al, (3) Mn-Co and (4) Na-Ca-Si-Mg-Fe and (5) REE-Ni-Zn. Measurements of FeOOH in massive sulphide samples are not included in the t-SNE analysis

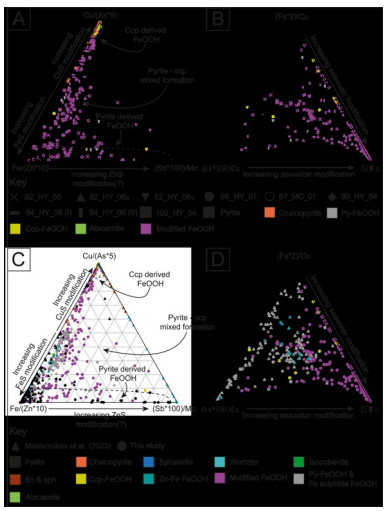

Fig. 9 Ternary discrimination diagrams of FeOOH precursors at Semenov, showing potential sources of post-formational modification. Diagrams (**A**) and (**C**) depict areas of pyrite (py) and chalcopyrite (ccp) derived FeOOH, a mixed signature, and possible ZnS modification. Diagrams (**B**) and (**D**) illustrate the modification of seawater interaction with FeOOH. (**A**) and (**B**) show data from this study, while (**C**) and (**D**) compare with LA-ICP-MS measurements of FeOOH from Pobeda vent field (Maslennikov et al. 2023). Fe sulphide FeOOH replaces py-FeOOH, indicating origins from Fe-sulphide (pyrite, pyrrhotite, marcasite), and Zn-Fe-FeOOH suggests derivation from Zn-Fe sulphide (e.g., wurtzite). Bn – bornite, sph – sphalerite. FeOOH with relict sulphide ablation omitted from diagrams

The fate of Au and Ag

Elevated concentrations of Au and Ag in SMS deposits may enable their valorisation as by-products of Cu and Zn extraction (Herzig and Hannington 1995; Hannington et al. 2010). Previous studies have reported native Au occurring within FeOOH, with FeOOH-dominated bulk samples containing concentration up to 28.4 ppm (Fouquet et al. 1993; Herzig et al. 1991; Maslennikov et al. 2023). While this study observes Au enrichment in py-FeOOH (median of 1.3 ppm) and Ag in ccp-FeOOH (25.5 ppm), correlations and ablation depth profiles show these enrichments are hosted by sulphide inclusions (Fig. 5E). Measurements of FeOOH with no sulphide inclusions and no spatial association with sulphide minerals contain median grades of <0.1 ppm Au and Ag (Fig. 4F). Depletion of Au and Ag in FeOOH cannot be explained by a Au-Ag-poor sulphide protolith, as sulphides in 82_HY_06 and 94_HY_06 (e.g., 06iiS5-7) have Au and Ag concentrations similar to this study's median. By contrast, modified FeOOH in 82_HY_06$_a$ and 94_HY_06 are depleted in both Au and Ag. Combined with the sharp contrast of Au and Ag between the sulphide phases and their alteration products (Fig. 12E and L), this suggests that precious metals are not trapped within FeOOH phases during seafloor weathering. The spatial association of Au and Ag with pyrite and chalcopyrite rims suggests that they precipitate rapidly at pH/Eh gradients generated where sulphide-derived acidic fluids mix with seawater at the oxidation front (Fig. 12D and J). As sulphides shrink during oxidation, Au and Ag remain bound to the sulphide rim. After complete oxidation, both Au and Ag are absent within resulting FeOOH, implying mobilisation after complete sulphide loss through oxidation.

To understand these observations, it is essential to consider how weathering processes in marine SMS deposits differ from those in terrestrial massive sulphide environments. In terrestrial deposits, Au and Ag are mobilised from oxidising sulphides by acidic meteoric waters (pH<5.5) as chloride complexes or under near-neutral conditions as thiosulphate complexes (Webster and Mann 1984). Thiosulphate/chloride complexes are transported downward through weathering profiles and precipitate at redox boundaries where oxidised fluids encounter reducing conditions, such as at the interface between oxidised gossans and underlying reduced lithologies (e.g., fresh sulphide; Mann 1984; Webster and Mann 1984; Yesares et al. 2014). In contrast, SMS deposits are influenced by seawater, buffering pH to ~8, limiting the development of highly acidic conditions favourable for efficient Au and Ag mobilisation as chloride complexes. While initial sulphide oxidation may generate locally acidic pore fluids capable of forming chloride

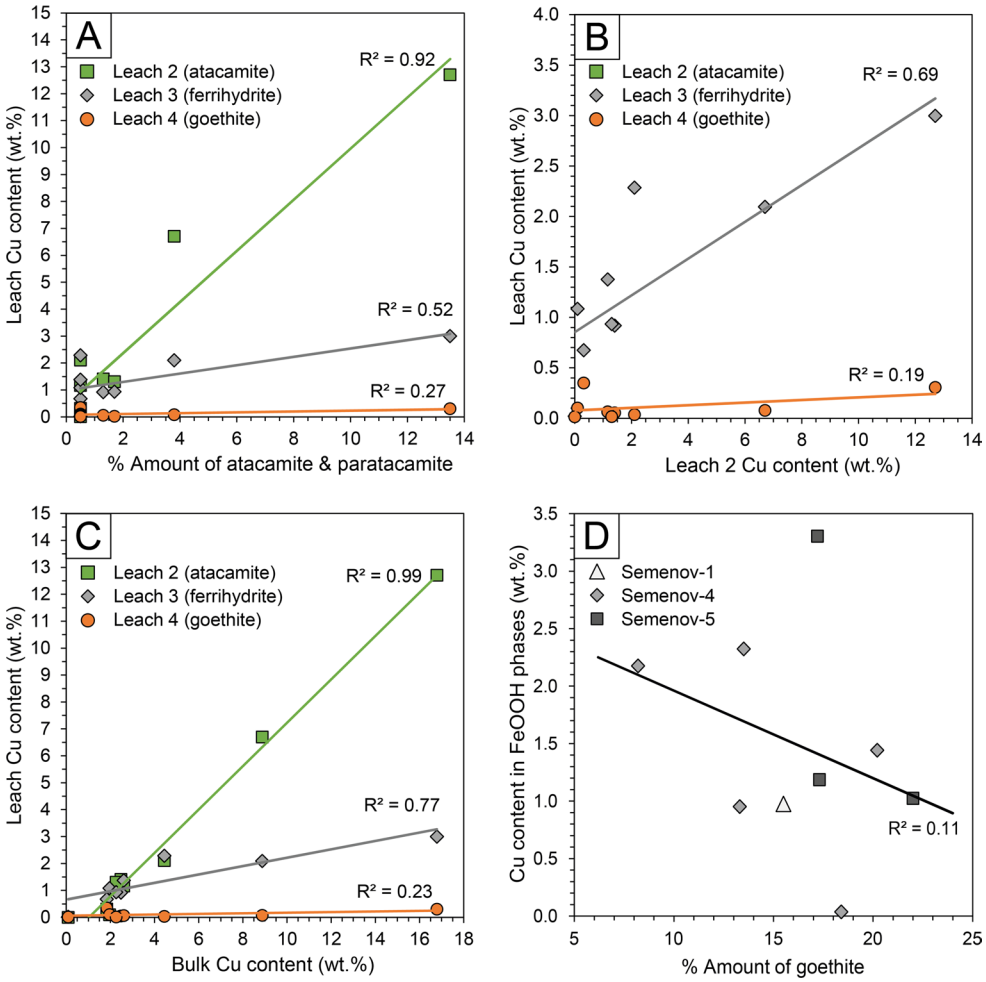

Fig. 10 Bivariate plots illustrating relationships relevant to Cu deportment in the samples. (**A**) Leached Cu content against the % amount of (par)atacamite by quantitative XRD. (**B**) Leached Cu content of leach 3 and leach 4 against the leached Cu content of leach 2. (**C**) Leached Cu content against the bulk Cu content of the sample and. (**D**) The Cu content within FeOOH phases (i.e., goethite and ferrihydrite) against the % amount of goethite in the sample by quantitative XRD

complexes (Rose 1976; Mann 1984; Hannington 1993), the buffering capacity of seawater likely restricts sustained acidic conditions, potentially favouring the formation of less mobile thiosulphate complexes instead (Webster 1986; Benedetti and Boulègue 1991).

The absence of Au and Ag in fully oxidised FeOOH samples at Semenov, despite previous findings of residual Au in seafloor samples of FeOOH elsewhere (Herzig et al. 1991) may reflect sampling within zones where seawater-buffered conditions were unsuitable for Au and Ag precipitation, suggesting their mobilisation after complete sulphide oxidation. The data from this study do not provide definitive insights into the ligands responsible for Au and Ag remobilisation in SMS deposits. Therefore, the following discussion explores potential transport mechanisms that may occur under seawater-dominated conditions and explain the observations of this study. During the final stages of sulphide oxidation, seawater dominated, near neutral and oxidising conditions likely dominate within FeOOH crust pore space. Under these conditions, intermediate thiosulphate ions produced by sulphide oxidation (Eq. 1) could mobilise Au or Ag as thiosulphate complexes (e.g., Eq. 2; Goldhaber 1983; Webster 1986). Thiosulphate complexes are stable under the pH and Eh conditions corresponding to goethite stability in seawater (Becking et al. 1960; Glasby and Schulz 1999; ESM 1.13), allowing their coexistence and mobilisation from FeOOH. Production of thiosulphate ions may also be facilitated by sulphide oxidising bacteria at hydrothermally inactive SMS deposits (Schippers et al. 1996; Reith et al. 2007; Sylvan et al. 2012). Thiosulphate complexes have reduced capacity to adsorb onto goethite relative to chloride complexes and this may explain the absence of Au (and likely Ag) within FeOOH phases (Ran et al. 2002).

$$FeS_2\ (s) + 6Fe^{3+} + 3H_2O\ = S_2O_3^{2-} + 7Fe^{2+} + 6H^+ \quad (1)$$

$$4Au + 8S_2O_3^{2-} + O_2 + 2H_2O = 4\left[Au(\,S_2O_3^{2-})_2\right]^{3-} + 4OH^- \quad (2)$$

The fate of mobilised Au-Ag thiosulphate complexes likely depends on fluid flow patterns within SMS deposits. In terrestrial massive sulphide deposits, Au and Ag mobilise through gravity-driven downward migration of fluids (Mann 1984). Whereas SMS deposits can experience complex fluid-flow patterns during their, including hydrothermal convection,

fracture-controlled circulation, and permeability contrasts (Rona 1984), although convection ceases once hydrothermal activity shuts down. The direction of fluid flow within the weathering system could determine the decomposition of thiosulphate complexes and subsequent Au-Ag precipitation (Webster 1986). Upward migration into oxic seawater or overlying carbonate-rich sediment should lead to thiosulphate oxidation and Au-Ag precipitation (Eq. 3; Kalinin et al. 2019), while downward migration and reduction within the SMS mound could also result in thiosulphate decomposition and Au-Ag precipitation (Webster 1986).

$$Au(S_2O_3)_2^{3-} + 2.5H_2O + 3.75O_2 = Au\,(s) + 4SO_4^{2-} + 5H^+ \quad (3)$$

While the fate of Au and Ag during sulphide weathering at SMS deposits remains an open question, the near complete absence of Au and Ag in FeOOH suggests that surface sampling of oxidised SMS deposits underestimate precious metal content of underlying sulphide. Moreover, downward migration of Au and Ag could result is supergene enrichment zones at the FeOOH-sulphide boundary. Future studies should aim to acquire preserved drill cores of FeOOH and underlying sulphides, as well as FeOOH-carbonate sediment interfaces, capturing both oxidised and fresh sulphides to enable a more detailed analysis of Au and Ag mobilisation, precipitation and possible supergene processes, particularly at redox boundaries and pH buffer interfaces.

Model for sulphide weathering, FeOOH formation and post-formational modification

This study presents a conceptual model illustrating the mineralogical and geochemical evolution of sulphides and their weathering products at SMS deposits (Fig. 11). Stage 1 shows primary, unaltered sulphides typical of young SMS deposits. Stage 2 depicts initial weathering, where chalcopyrite oxidises before pyrite (Fig. 3D), likely driven by galvanic interactions (Knight et al. 2018; Fallon et al. 2017; Mehta and Murr 1983). Chalcopyrite oxidation forms covellite, with expelled Fe precipitating as ccp-FeOOH and inheriting chalcopyrite's geochemical signature. Mobilised Ag becomes enriched in covellite or binds to the grain boundaries of chalcopyrite. Stage 3 involves pyrite oxidation, forming py-FeOOH, with Au and Ag bound at pyrite rims. Continued Cu-sulphide oxidation releases Cu^{2+} ions that are later precipitated as atacamite or incorporated into FeOOH. In Stage 4, sulphides are fully oxidised. Seawater-dominated interaction depletes sulphide-derived elements (e.g., Zn, As, Sb) and enriches seawater-derived elements (e.g., Na, Si, Ca, REEs). Goethite crystallisation from ferrihydrite re-releases Cu and Zn which may adsorb onto neighbouring FeOOH. Goethite crystallisation may occur more rapidly in py-FeOOH that contains lower Cu and higher Fe relative to ccp-FeOOH (Jambor and Dutrizac 1998). By Stage 5, the FeOOH has been modified by continued seawater interaction and has adsorbed metals released from nearby oxidising sulphides. This results in a modified FeOOH phase that obscures the original sulphide-derived composition. The long-term fate of Cu and Zn beyond this stage remains unresolved (Fig. 11).

While this model advances our understanding of the compositional evolution of SMS deposits, several limitations exist. Data on the weathering of other sulphides (e.g., sphalerite, marcasite, pyrrhotite) under ambient seawater conditions is limited, particularly regarding their contribution to FeOOH formation and composition, and the redistribution of metals such as Zn from Fe-poor phases (e.g., sphalerite, covellite) during weathering (Firstova et al. 2016; Lehrmann et al. 2022; Maslennikov et al. 2023). Some alteration products, such as jarosite and hematite, are not included due to their absence in our sample set (Herzig et al. 1991; Dutrieux 2020). Microbial influences including recently discovered "cable" bacteria forming galvanic coupling, also impact weathering dynamics (Mehta and Murr 1983; Toner et al. 2009; Meysman 2018). The rate of goethite crystallisation and its impact on FeOOH metal content is also yet to be fully considered. Finally, we have shown that the fate of Au and Ag during seafloor weathering of SMS is more complex than previously thought (e.g., Herzig et al. 1991). Whether these precious metals are retained or lost depends on whether fluids migrate downward to the sulphide-FeOOH boundary or upwards into seawater and will require sub-surface sampling and more detailed hydrodynamic consideration of SMS mounds to solve.

Implications of FeOOH and atacamite as an additional resource or exploration tool at SMS deposits

The average Cu content in bulk FeOOH with and without atacamite observed in this study (4.53 wt%, $n = 9$) and others (e.g., Herzig et al. 1991; Melekestseva et al. 2018; Hu et al. 2022) is comparable to those of volcanogenic massive sulphide (VMS) deposits (1.10–2.04 wt%; Barrie and Hannington 1999). Although atacamite comprises only a minor fraction of our samples compared to FeOOH (typically < 10%), its abundance shows the strongest correlation with bulk Cu content ($R^2 = 0.99$; Fig. 10C) where it also hosts the majority (60%) of the total Cu, averaging 2.87 wt% (Fig. 7). The presence of atacamite veins demonstrates mobilisation of Cu-rich fluids, and our leaching experiments show a positive correlation between atacamite abundance and Cu content in ferrihydrite ($R^2 = 0.69$), indicating that FeOOH adsorbs Cu from acidic solutions before atacamite

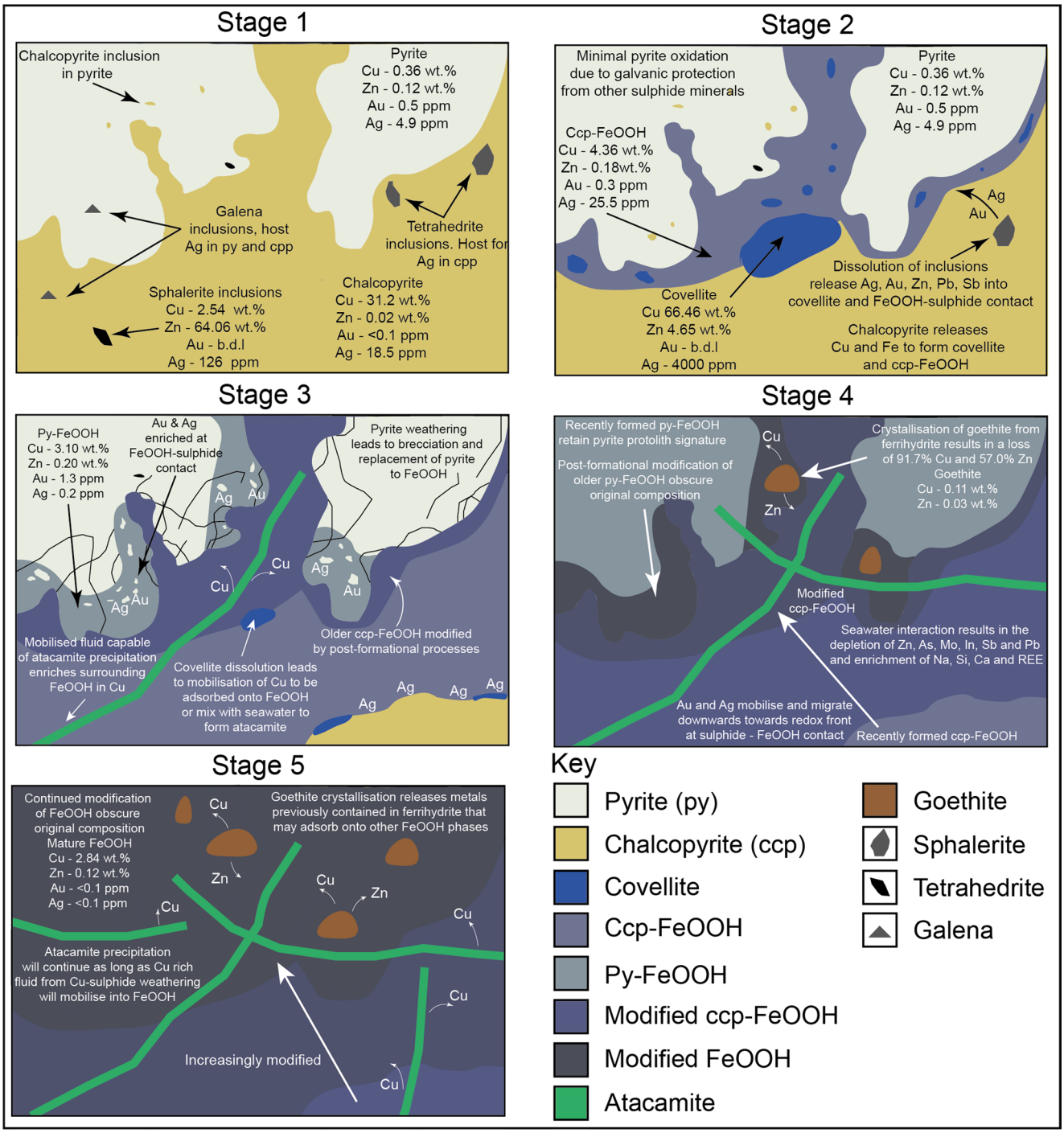

Fig. 11 Schematic illustration of SMS deposit evolution and associated geochemical changes. Stage 1: Formation of unoxidised sulphides. Stage 2: Minor oxidation of chalcopyrite forms covellite and ccp-FeOOH. Stage 3: Pyrite oxidation forms py-FeOOH, with Cu-sulphide weathering releasing Cu and enriching FeOOH via adsorption and atacamite precipitation. Stage 4: Complete sulphide oxidation drives Au and Ag migration, while seawater interaction enriches FeOOH in Na, Si, Ca, and REEs and depletes sulphide derived Zn, As, Mo, In, Sb and Pb. Stage 5: Post-formational processes obscure the sulphide protolith, with ongoing goethite crystallisation releasing Cu and Zn that may adsorb onto surrounding FeOOH

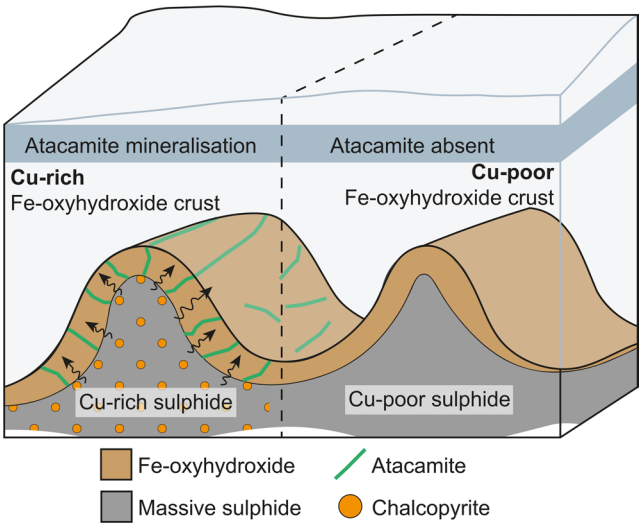

Fig. 12 Schematic diagram illustrating Cu-rich FeOOH deposits and atacamite mineralisation form by the weathering of Cu-rich sulphide and may indicate the underlying presence of Cu-rich sulphide in contrast to Cu-poor sulphide resulting in the formation of Cu-poor FeOOH deposits and a lack of atacamite mineralisation

precipitation occurs at higher pH when these fluids mix with seawater. Therefore, atacamite mineralisation may mark zones where Cu-rich fluids have migrated through the FeOOH crust, enriching the FeOOH in Cu prior to atacamite precipitation. Although not guaranteed to indicate fresh sulphide below, atacamite marks Cu-rich areas worth focusing on for exploring ageing, weathered SMS deposits (Fig. 12). Zinc content in bulk FeOOH is low (average of 0.16 wt%), but other SMS deposits, such as Yuhuang-1 (1.37 wt% Zn; Hu et al. 2022), show comparable Zn levels to VMS deposits (1.82–5.63 wt%; Barrie and Hannington 1999). Sequential leaching also demonstrates Zn is better retained than Cu during goethite crystallisation, losing only 57.0% Zn compared to 91.7% for Cu. As such, older SMS deposits may retain Zn-rich goethite.

In summary, samples of FeOOH and atacamite at Semenov exhibit Cu and occasionally Zn grades comparable to those found at VMS deposits; however, this comparison serves only as a benchmark and does not imply resource potential. The economic potential of FeOOH and atacamite remains uncertain due to limited knowledge of their grade and tonnage at SMS deposits. Nonetheless, atacamite may also serve as an exploration tool, providing targets for Cu-rich FeOOH and as a possible indicator for underlying Cu-rich massive sulphide.

Summary and conclusions

This study examined both minimally modified FeOOH in actively oxidising sulphide and modified FeOOH in fully oxidised sulphide to track their geochemical evolution. Initially, FeOOH inherits the elemental signature of its sulphide precursor, but progressive seawater interaction later depletes sulphide-derived elements (e.g., As, Sb) while enriching it with seawater-derived elements (e.g., Si, Ca, REEs). As sulphides oxidise, economic metals like Cu are released and adsorbed onto FeOOH, enriching it in Cu before (par)atacamite precipitation. The mineralisation of (par)atacamite can be used for a dual purpose: as a possible exploration tool for underlying Cu-rich massive sulphide and to highlight surrounding Cu-rich oxidised FeOOH crust. Although our data indicates that ferrihydrite crystallisation to goethite may lower metal tenor (with losses of 91.7% Cu and 57.0% Zn from ferrihydrite), goethite crystallisation may not be extensive and the released Cu and Zn may re-adsorb onto adjacent FeOOH phases, potentially limiting metal loss at the deposit scale.

In contrast to the behaviours of Cu and Zn, LA-TOF-ICP-MS reveal that Au and Ag are bound to sulphide rims during oxidation and occur only at low concentrations in both FeOOH and atacamite. While the fate of these precious metals after complete sulphide oxidation remains an open question, we propose that Au and Ag may be mobilised via thiosulphate complexes to either seawater, FeOOH-carbonate sediment boundary or to the FeOOH-sulphide boundary deeper within the SMS mound. If the latter occurs, our data predict Au and Ag supergene enrichment at these boundaries.

Our schematic model summarises the geochemical evolution of SMS deposits, highlighting seafloor FeOOH crusts as long-term base metal traps, acting as a ‘marine gossan’. These findings imply that older, extinct, off-axis SMS deposits may still host economic metals locked within their alteration products. Consequently, our research not only advances the understanding of metal mobility during sulphide oxidation and the geochemical evolution of FeOOH but also provides a basis for the exploration of SMS deposits off-axis. Further research is needed on the fate of Au and Ag, goethite recrystallisation kinetics, tonnage estimates of weathering products, and processing methods for FeOOH and atacamite to fully assess their resource potential.

Supplementary Information The online version contains supplementary material available at https://doi.org/10.1007/s00126-026-01468-x.

Acknowledgements The authors would like to thank the James Cook JC224 Captain and crew, shipboard science party and the HyBIS technical support team for their assistance during the expedition. The authors also thank the ROV technical support team from the "ODEMAR" project and Sven Petersen (GEOMAR) for providing the bathymetry maps from the Semenov hydrothermal cluster. We thank Simon Chenery (British Geological Survey), Matt Cooper (University of Southampton), Kate Peel (National Oceanography Centre) and Richard Pearce (University of Southampton) for their help with geochemical analyses and Berit Lehrmann for the use of her microscope for petrographical analyses.

Author contributions Christian Bishop: Conceptualisation, data curation, formal analysis, investigation, methodology, writing. Pierre Josso: Conceptualisation, writing – review and editing. Bramley Murton: Conceptualisation, seagoing expedition leader, supervision, writing – review and editing. Anna Lichtschlag: Supervision, writing – review & editing. Stephen Roberts: Supervision, writing – review and editing. Thomas Belgrano: Resource provision, Writing – Review and editing. J. Andy Milton: Methodology, investigation. Maxime Lesage: Supervision, writing – review.

Funding This study was funded by the Natural Environment Research Council (NERC) through "Project ULTRA" (grant number NE/S004068/1). This work was supported by a PhD studentship funded by Green Minerals.

Data availability The data used within this study are available within the electronic supplementary material, with data also stored in BODC database via https://doi.org/10.5285/3724bb78-2139-edbe-e063-7086abc0903f after Bishop et al. (2025d), raw LA-ICP-MS and image data via https://doi.org/10.5285/373699c7-6323-d4fa-e063-7086abc08606 after Bishop et al. (2025e) and raw LA-TOF-ICP-MS via https://doi.org/10.5285/37352554-2193-8984-e063-7086abc047f5 after Bishop et al. (2025f).

Declarations

Conflict of interest While Green Minerals provided financial support to Bishop (PhD stipend) and employs Lesage, the authors declare that they have no known competing financial interests or personal relationships that could have appeared to influence the work reported in this paper.

References

Barrie CT, Hannington MD (1999) Volcanic-associated massive sulfide deposits: Processes and examples in modern and ancient settings. Rev Econ Geol 8:1–11

Becking LGMB, Kaplan IR, Moore D (1960) Limits of the natural environment in terms of pH and oxidation-reduction potentials. J Geol 68:243–284. https://doi.org/10.1086/626659

Beltenev V, Ivanov A, Rozhdestvenskaya I, Cherkashov G, Stepanova T, Shilov V, Davydov M, Laiba A, Kaylio V, Narkevsky E, Pertsev A, Dobretzova I, Gustaytis A, Popova Y, Amplieva E, Evrard C (2009) New data about hydrothermal fields on the Mid-Atlantic Ridge between 11°–14°N: 32nd Cruise of R/V Professor Logatchev. InterRidge News 18:13–17

Beltenev V, Ivanov A, Rozhdestvenskaya I, Cherkashov G, Stepanova T, Shilov V, Pertsev A, Davydov M, Egorov I, Melekestseva I, Narkevsky E, Ignatov V (2007) A new hydrothermal field at 13°30′N on the Mid-Atlantic Ridge. InterRidge News 16:9–10

Benedetti M, Boulëgue J (1991) Mechanism of gold transfer and deposition in a supergene environment. Geochim Cosmochim Acta 55:1539–1547. https://doi.org/10.1016/0016-7037(91)90126-P

Bishop C, Lichtschlag A, Roberts S, Lesage M, Murton BJ (2025a) Fe-oxyhydroxide deposits at Semenov hydrothermal field (13°30′N), Mid-Atlantic ridge: insights into formation, modification and resource potential. Miner Deposita. https://doi.org/10.1007/s00126-025-01376-6

Bishop C, Murton B, Lichtschlag A, Roberts S (2025b) Images and descriptions of Fe-oxyhydroxide and massive sulphide samples from Semenov Hydrothermal Field of the Mid-Atlantic Ridge during the RRS James Cook cruise JC224 (March–April 2022). NERC EDS British Oceanographic Data Centre NOC. https://doi.org/10.5285/2e0a9d33-56f6-622d-e063-7086abc06e59

Bishop C, Murton B, Lichtschlag A, Roberts S (2025c) Geochemical composition, isotopic measurements and X-ray diffraction (XRD) results of Fe-oxyhydroxide and massive sulphide samples from Semenov Hydrothermal Field of the Mid-Atlantic Ridge during the RRS James Cook cruise JC224 (March–April 2022). NERC EDS British Oceanographic Data Centre NOC. https://doi.org/10.5285/2e0aa2c7-6331-62b9-e063-7086abc06891

Bishop C, Josso P, Lichtschlag A, Roberts S, Belgrano T, Milton J, Lesage M, Murton B (2025d) Geochemical analyses, sequential leaching and X-ray diffraction (XRD) results of Fe-oxyhydroxide and massive sulphide samples from the Semenov Hydrothermal Field, Mid-Atlantic Ridge, during RRS James Cook cruise JC224 (March-April 2022). NERC EDS British Oceanographic Data Centre NOC. https://doi.org/10.5285/3724bb78-2139-edbe-e063-7086abc0903f

Bishop C, Josso P, Lichtschlag A, Roberts S, Belgrano T, Lesage M, Murton B (2025e) Raw laser-ablation inductively couple plasma mass spectrometer (LA-ICP-MS) data and images of laser-ablation (LA) targets of Fe-oxyhydroxide and massive sulphide samples from the Semenov Hydrothermal Field of the Mid-Atlantic Ridge during the RRS James Cook cruise JC224 (March-April 2022). NERC EDS British Oceanographic Data Centre NOC. https://doi.org/10.5285/373699c7-6323-d4fa-e063-7086abc08606

Bishop C, Josso P, Lichtschlag A, Roberts S, Belgrano T, Milton J, Lesage M, Murton B (2025f) Raw laser-ablation time-of-flight inductively couple plasma mass spectrometer (LA-TOF-ICP-MS) data from sample 82_HY_06 from the Semenov Hydrothermal Field of the Mid-Atlantic Ridge during the RRS James Cook cruise JC224 (March-April 2022). NERC EDS British Oceanographic Data Centre NOC. https://doi.org/10.5285/37352554-2193-8984-e063-7086abc047f5

Blowes DW, Ptacek CJ, Jambor JL, Weisener CG (2003) The geochemistry of acid mine drainage. In: Holland HD, Turekian KK (eds) Treatise on Geochemistry. Pergamon, Oxford, pp 149–204

Brinza L, Vu HP, Neamtu M, Benning LG (2019) Experimental and simulation results of the adsorption of Mo and V onto ferrihydrite. Sci Rep 9:1365. https://doi.org/10.1038/s41598-018-37875-y

Cherkashov G, Kuznetsov V, Kuksa K, Tabuns E, Maksimov F, Beltenev V (2017) Sulfide geochronology along the Northern Equatorial Mid-Atlantic Ridge. Ore Geol Rev 87:63–74. https://doi.org/10.1016/j.oregeorev.2016.10.015

Chesne RB, Kim CS (2014) Zn(II) and Cu(II) adsorption and retention onto iron oxyhydroxide nanoparticles: effects of particle aggregation and salinity. Geochem Trans 15:6. https://doi.org/10.1186/1467-4866-15-6

Claff S, Sullivan L, Burton E, Bush R (2010) A sequential extraction procedure for acid sulfate soils: Partitioning of iron. Geoderma 155:224–230. https://doi.org/10.1016/j.geoderma.2009.12.002

Cornell RM, Schwertmann U (2003) The iron oxides: Structure, properties, reactions, occurrences and uses, 2nd edn. Wiley-VCH, Weinheim. https://doi.org/10.1002/3527602097

Davis CC, Chen H-W, Edwards M (2002) Modeling Silica Sorption to Iron Hydroxide. Environ Sci Technol 36:582–587. https://doi.org/10.1021/es010996t

Debaar HJW, Bacon MP, Brewer PG, Bruland KW (1985) Rare-earth elements in the Pacific and Atlantic Oceans. Geochim Cosmochim Acta 49:1943–1959. https://doi.org/10.1016/0016-7037(85)90089-4

Dekov V, Boycheva T, Halenius U, Petersen S, Billstrom K, Stummeyer J, Kamenov G, Shanks W (2011) Atacamite and paratacamite from the ultramafic-hosted Logatchev seafloor vent field (14°45′N, Mid-Atlantic Ridge). Chem Geol 286:169–184. https://doi.org/10.1016/j.chemgeo.2011.05.002

Dileep Kumar M (1981) The oxidation state diagram: stability of dissolved sulphur species in seawater. Mar Chem 10:475–486. https://doi.org/10.1016/0304-4203(81)90002-5

Dong A, Sun Z, Kendall B, Izon G, Cao H, Li Z, Ma X, Yin X, Qiu Z, Zhu X-K, Bekker A, Poulton SW (2022) Insights from modern diffuse-flow hydrothermal systems into the origin of post-GOE deep-water Fe–Si precipitates. Geochim Cosmochim Acta 317:1–17. https://doi.org/10.1016/j.gca.2021.10.001

Dutrieux MA (2020) Rise and fall of a hydrothermal system: a tale of metalliferous sediments (TAG hydrothermal field, MAR, 26°N). PhD Thesis, University of Southampton, pp 286

Eggins SM, Shelley JMG (2002) Compositional heterogeneity in NIST SRM 610–617 glasses. Geostand Newsl 26:269–286. https://doi.org/10.1111/j.1751-908X.2002.tb00634.x

Elderfield H, Hawkesworth CJ, Greaves MJ, Calvert SE (1981) Rare earth element geochemistry of oceanic ferromanganese nodules and associated sediments. Geochim Cosmochim Acta 45:513–528. https://doi.org/10.1016/0016-7037(81)90184-8

Emmons WH (1917) The enrichment of ore deposits. US Geol Surv Bull 625. https://pubs.usgs.gov/publication/b625

Erickson BE, Helz GR (2000) Molybdenum(VI) speciation in sulfidic waters: Stability and lability of thiomolybdates. Geochim Cosmochim Acta 64:1149–1158. https://doi.org/10.1016/S0016-7037(99)00423-8

Escartin J (2014) ODEMAR oceanic detachment faults at the Mid-Atlantic Ridge. Cruise Report. N/O Pourquoi pas? – ROV Victor 6000 – AUV Abyss 6000. 16 Nov – 19 Dec 2013, Mindelo (Cape Verde) - Point a Pitre (Guadeloupe). https://doi.org/10.13155/47149

Fallon EK, Petersen S, Brooker RA, Scott TB (2017) Oxidative dissolution of hydrothermal mixed-sulphide ore: An assessment of current knowledge in relation to seafloor massive sulphide mining. Ore Geol Rev 86:309–337. https://doi.org/10.1016/j.oregeorev.2017.02.028

Firstova A, Cherkashov G, Stepanova T, Sukhanova A, Poroshina I, Bel'tenev V (2022) New data for the internal structure of ultramafic hosted seafloor massive sulfides (SMS) deposits: Case study of the Semenov-5 hydrothermal field (13°31′N, MAR). Minerals 12:1593. https://doi.org/10.3390/min12121593

Firstova A, Stepanova T, Cherkashov G, Goncharov A, Babaeva S (2016) Composition and formation of gabbro-peridotite hosted seafloor massive sulfide deposits from the Ashadze-1 hydrothermal field, Mid-Atlantic Ridge. Minerals 6:19. https://doi.org/10.3390/min6010019

Firstova A, Stepanova T, Sukhanova A, Cherkashov G, Poroshina I (2019) Au and Te minerals in seafloor massive sulphides from Semyenov-2 hydrothermal field, Mid-Atlantic Ridge. Minerals 9:294. https://doi.org/10.3390/min9050294

Fouquet Y, Wafik A, Cambon P, Mevel C, Meyer G, Gente P (1993) Tectonic setting and mineralogical and geochemical zonation in the Snake Pit sulfide deposit (Mid-Atlantic Ridge at 23°N). Econ Geol 88:2018–2036. https://doi.org/10.2113/gsecongeo.88.8.2018

Garbe-Schönberg D, Müller S (2014) Nano-particulate pressed powder tablets for LA-ICP-MS. J Anal Spectrom 29:990–1000. https://doi.org/10.1039/C4JA00007B

Gini C, Jamieson JW, Reeves EP, Gartman A, Barreyre T, Babechuk MG et al (2024) Iron oxyhydroxide-rich hydrothermal deposits at the high-temperature Fåvne vent field, Mohns Ridge. Geochem Geophys Geosyst 25:e2024GC011481. https://doi.org/10.1029/2024GC011481

Glasby GP, Schulz HD (1999) Eh-pH diagrams for Mn, Fe, Co, Ni, Cu and As under seawater conditions: Application of two new types of Eh-pH diagrams to the study of specific problems in marine geochemistry. Aquat Geochem 5:227–248. https://doi.org/10.1023/A:1009663322718

Goldhaber M (1983) Experimental study of metastable sulfur oxyanion formation during pyrite oxidation at pH 6–9 and 30°C. Am J Sci 283:193–217. https://doi.org/10.2475/ajs.283.3.193

Görn MG, Bolanz RM, Parry S et al (2021) Incorporation of Mo6+in ferrihydrite, goethite, and hematite. Clays Clay Min 69:188–204. https://doi.org/10.1007/s42860-021-00116-x

Grant JA (1986) The isocon diagram; a simple solution to Gresens' equation for metasomatic alteration. Econ Geol 81:1976–1982. https://doi.org/10.2113/gsecongeo.81.8.1976

Gresens RL (1967) Composition-volume relationships of metasomatism. Chem Geol 2:47–65. https://doi.org/10.1016/0009-2541(67)90004-6

Grundl T, Delwiche J (1993) Kinetics of ferric oxyhydroxide precipitation. J Contam Hydrol 14:71–87. https://doi.org/10.1016/0169-7722(93)90042-Q

Hannington MD (1993) The formation of atacamite during weathering of sulfides on the modern sea floor. Can Mineral 31:945–956

Hannington MD, Jamieson J, Monecke T, Petersen S (2010) Modern sea-floor massive sulfides and base metal resources: toward an estimate of global sea-floor massive sulfide potential. In: Goldfarb RJ, Marsh EE, Monecke T (eds) The challenge of finding new mineral resources: Global metallogeny, innovative exploration, and new discoveries, vol 2. Zinc–lead, nickel–copper–PGE, and uranium. Soc Econ Geol Spec Publ 15:317–338. https://doi.org/10.5382/SP.15.2.001

Hekinian R, Hoffert M, Larque P, Cheminee JL, Stoffers P, Bideau D (1993) Hydrothermal Fe and Si oxyhydroxide deposits from South Pacific intraplate volcanos and East Pacific Rise axial and off-axial regions. Econ Geol 88:2099–2121. https://doi.org/10.2113/gsecongeo.88.8.2099

Hepburn LE, Butler IB, Boyce A, Schröder C (2020) The use of operationally-defined sequential Fe extraction methods for mineralogical applications: A cautionary tale from Mössbauer spectroscopy. Chem Geol 543:119584. https://doi.org/10.1016/j.chemgeo.2020.119584

Herzig PM, Hannington MD (1995) Polymetallic massive sulfides at the modern seafloor: A review. Ore Geol Rev 10:95–115. https://doi.org/10.1016/0169-1368(95)00009-7

Herzig PM, Hannington MD, Scott SD, Maliotis G, Rona PA, Thompson G (1991) Gold-rich sea-floor gossans in the Troodos Ophiolite and on the Mid-Atlantic Ridge. Econ Geol 86:1747–1755. https://doi.org/10.2113/gsecongeo.86.8.1747

Hou X, Han X, Hu X, Liu J (2024) Formation mechanism of Fe oxyhydroxides and behavior of metals during the oxidation of submarine sulfides at the Wocan-1 hydrothermal field, Carlsberg Ridge. Ore Geol Rev 174:106307. https://doi.org/10.1016/j.oregeorev.2024.106307

Hu S, Tao C, Liao S, Guan Y, Yin X, Zhu C, Liang J, Guo Z (2023) Oxidative dissolution of sulfide minerals tends to accumulate more dissolved heavy metals in deep seawater environments than in shallow seawater environments. Environ Sci Technol 57:21438–21447. https://doi.org/10.1021/acs.est.3c07507

Hu S, Tao C, Liao S, Zhu C, Qiu Z (2022) Transformation of minerals and mobility of heavy metals during oxidative weathering of seafloor massive sulfide and their environmental significance. Sci Total Environ 819:153091. https://doi.org/10.1016/j.scitotenv.2022.153091

Jambor JL, Dutrizac JE (1998) Occurrence and constitution of natural and synthetic ferrihydrite, a widespread iron oxyhydroxide. Chem Rev 98:2549–2586. https://doi.org/10.1021/cr970105t

Jochum KP, Nohl U, Herwig K, Lammel E, Stoll B, Hofmann AW (2005) GeoReM: A new geochemical database for reference materials and isotopic standards. Geostand Geoanal Res 29:333–338. https://doi.org/10.1111/j.1751-908X.2005.tb00904.x

Jochum KP, Wilson SA, Becker H, Garbe-Schönberg D, Groschopf N, Kadlag Y, Macholdt DS, Mertz-Kraus R, Otter LM, Stoll B, Stracke A, Weis U, Haug GH, Andreae MO (2016) FeMnOx-1: A new microanalytical reference material for the investigation of Mn–Fe rich geological samples. Chem Geol 432:34–40. https://doi.org/10.1016/j.chemgeo.2016.03.026

Johnson NE, Craig JR, Rimstidt JD (1986) Compositional trends in tetrahedrite. Can Mineral 24:385–397

Kaiser HF (1974) An index of factorial simplicity. Psychometrika 39:31–36. https://doi.org/10.1007/BF02291575

Kalinin YA, Palyanova GA, Naumov EA, Kovalev KR, Pirajno F (2019) Supergene remobilization of Au in Au-bearing regolith related to orogenic deposits: A case study from Kazakhstan. Ore Geol Rev 109:358–369. https://doi.org/10.1016/j.oregeorev.2019.04.019

Kennedy CB, Scott SD, Ferris FG (2004) Hydrothermal phase stabilization of 2-line ferrihydrite by bacteria. Chem Geol 212:269–277. https://doi.org/10.1016/j.chemgeo.2004.08.017

Knight RD, Roberts S, Cooper MJ (2018) Investigating monomineralic and polymineralic reactions during the oxidation of sulphide minerals in seawater: Implications for mining seafloor massive sulphide deposits. Appl Geochem 90:63–74. https://doi.org/10.1016/j.apgeochem.2017.12.027

Krijthe JH (2015) Rtsne: T-distributed stochastic neighbor embedding using Barnes-Hut implementation. R package version 0.17. https://github.com/jkrijthe/Rtsne

Kuznetsov V, Maksimov F, Zheleznov A, Cherkashov G, Bel'tenev V, Lazareva L (2011) Th-230/U chronology of ore formation within the Semyenov hydrothermal district (13°31′N) at the Mid-Atlantic Ridge. Geochronometria 38:72–76. https://doi.org/10.2478/s13386-011-0001-1

Lehrmann B, Cooper MJ, Milton JA, Murton BJ (2022) Formation, remobilisation and alteration processes at inactive hydrothermal vents: Insights from elemental analysis of Cu-(Fe-)S sulfides from TAG, Mid-Atlantic Ridge. Miner Deposita 57:1431–1448. https://doi.org/10.1007/s00126-022-01106-2

MacLeod CJ, Searle RC, Murton BJ, Casey JF, Mallows C, Unsworth SC, Achenbach KL, Harris M (2009) Life cycle of oceanic core complexes. Earth Planet Sci Lett 287:333–344. https://doi.org/10.1016/j.epsl.2009.08.016

MacQueen JB (1967) Some methods for classification and analysis of multivariate observations. In: Le Cam LM, Neyman J (eds) Proc 5th Berkeley Symp Math Stat Prob, vol 1. University of California Press, Berkeley, pp 281–297. http://projecteuclid.org/euclid.bsmsp/1200512992

Maechler M, Rousseeuw P, Struyf A, Hubert M, Hornik K (2023) Cluster: cluster analysis basics and extensions. R package version 2.1.6. https://CRAN.R-project.org/package/cluster

Mann AW (1984) Mobility of gold and silver in lateritic weathering profiles: Some observations from Western Australia. Econ Geol 79:38–49. https://doi.org/10.2113/gsecongeo.79.1.38

Mann HB, Whitney DR (1947) On a test of whether one of two random variables is stochastically larger than the other. Ann Math Stat 18:50–60

Maslennikov VV, Cherkashov GA, Firstova AV, Ayupova NR, Beltenev VE, Melekestseva IY, Artemyev DA, Tseluyko AS, Blinov IA (2023) Trace element assemblages of pseudomorphic iron oxyhydroxides of the Pobeda-1 hydrothermal field, 17°08.7′N, Mid-Atlantic Ridge: The development of a halmyrolysis model from LA-ICP-MS data. Minerals 13:4. https://doi.org/10.3390/min13010004

McKnight PE, Najab J (2010) Mann–Whitney U test. In: Weiner IB, Craighead WE (eds) The Corsini Encyclopedia of Psychology. Wiley, New Jersey

McLennan SM (1989) Rare earth elements in sedimentary rocks: Influence of provenance and sedimentary processes. In: Lipin BR, McKay GA (eds) Geochemistry and mineralogy of rare earth elements. De Gruyter, Berlin, pp 169–200. https://doi.org/10.1515/9781501509032-010

Mehta AP, Murr LE (1983) Fundamental studies of the contribution of galvanic interaction to acid-bacterial leaching of mixed metal sulfides. Hydrometallurgy 9:235–256. https://doi.org/10.1016/0304-386X(83)90025-7

Melekestseva I, Maslennikov VV, Safina NP, Nimis P, Maslennikova S, Beltenev V, Rozhdestvenskaya I, Danyushevsky L, Large R, Artemyev D, Kotlyarov V, Toffolo L (2018) Sulfide breccias from the Semenov-3 hydrothermal field, Mid-Atlantic Ridge: Authigenic mineral formation and trace element pattern. Minerals 8:321. https://doi.org/10.3390/min8080321

Melekestseva IY, Maslennikov VV, Ayupova NR, Belogub EV, Maslennikova SP, Bel'tenev VE, Danyushevsky L, Large R (2020) Behavior of Trace Elements during Oxidation of Sphalerite of the Irinovskoe Hydrothermal Sulfide Field (13 degrees 20 ' N, Mid-Atlantic Ridge). Geol Ore Depos 62:254–259. https://doi.org/10.1134/S1075701520030058

Melekestseva IY, Maslennikov VV, Maslennikova SP, Danyushevsky LV, Large R (2017) Covellite of the Semenov-2 hydrothermal field (13A degrees 31.13' N, Mid-Atlantic Ridge): Enrichment in trace elements according to LA ICP MS analysis. Dokl Earth Sci 473:291–295. https://doi.org/10.1134/S1028334x17030060

Melekestseva IY, Tret'yakov GA, Nimis P, Yuminov AM, Maslennikov VV, Maslennikova SP, Kotlyarov VA, Beltenev VE, Danyushevsky LV, Large R (2014) Barite-rich massive sulfides from the Semenov-1 hydrothermal field (Mid-Atlantic Ridge, 13 degrees 30.87 ' N): Evidence for phase separation and magmatic input. Mar Geol 349:37–54. https://doi.org/10.1016/j.margeo.2013.12.013

Mendez JC, Hiemstra T (2020) Ternary Complex Formation of Phosphate with Ca and Mg Ions Binding to Ferrihydrite: Experiments and Mechanisms. ACS Earth Space Chem 4:545–557. https://doi.org/10.1021/acsearthspacechem.9b00320

Meysman FJR (2018) Cable bacteria take a new breath using long-distance electricity. Trends Microbiol 26:411–422. https://doi.org/10.1016/j.tim.2017.10.011

Mills RA, Elderfield H (1995) Rare earth element geochemistry of hydrothermal deposits from the active TAG Mound, 26°N Mid-Atlantic Ridge. Geochim Cosmochim Acta 59:3511–3524. https://doi.org/10.1016/0016-7037(95)00224-N

Moon EM, Peacock CL (2012) Adsorption of Cu(II) to ferrihydrite and ferrihydrite–bacteria composites: Importance of the carboxyl group for Cu mobility in natural environments. Geochim Cosmochim Acta 92:203–219. https://doi.org/10.1016/j.gca.2012.06.012

Murton BJ, Hühnerbach V, Gattard J (2012) HyBIS: A new concept in versatile, 6000-m rated robotic underwater vehicles. In: Griffiths G (ed) Further advances in unmanned marine vehicles. IET, London. https://doi.org/10.1049/PBCE077E_ch3

Namayandeh A, Borkiewicz OJ, Bompoti NM, Chrysochoou M, Michel FM (2022) Oxyanion Surface Complexes Control the Kinetics and Pathway of Ferrihydrite Transformation to Goethite and Hematite. Environ Sci Technol 56:15672–15684. https://doi.org/10.1021/acs.est.2c04971

Parfitt RL, Van der Gaast SJ, Childs CW (1992) A Structural Model for Natural Siliceous Ferrihydrite. Clays Clay Min 40:675–581. https://doi.org/10.1346/CCMN.1992.0400607

Paton C, Hellstrom J, Paul B, Woodhead J, Hergt J (2011) Iolite: Freeware for the visualisation and processing of mass spectrometric data. J Anal Spectrom 26:2508–2518. https://doi.org/10.1039/C1JA10172B

Paul B, Petrus J, Savard D, Woodhead J, Hergt J, Greig A, Paton C, Rayner P (2023) Time-resolved trace element calibration strategies for LA-ICP-MS. J Anal Spectrom 38:1995–2006. https://doi.org/10.1039/D3JA00037K

Pertsev AN, Bortnikov NS, Vlasov EA, Beltenev VE, Dobretsov IG, Ageeva OA (2012) Recent massive sulfide deposits of the Semenov ore district, Mid-Atlantic Ridge, 13°31′N: Associated rocks of the oceanic core complex and their hydrothermal alteration. Geol Ore Deposits 54:334–346. https://doi.org/10.1134/S1075701512050030

Pollard AM, Thomas RG, Williams PA (1989) Synthesis and stabilities of the basic copper(II) chlorides atacamite, paratacamite and botallackite. Mineral Mag 53:557–563. https://doi.org/10.1180/minmag.1989.053.373.06

Poulton SW, Canfield DE (2005) Development of a sequential extraction procedure for iron: Implications for iron partitioning in continentally derived particulates. Chem Geol 214:209–221. https://doi.org/10.1016/j.chemgeo.2004.09.003

Ran Y, Fu J, Rate AW, Gilkes RJ (2002) Adsorption of Au(I, III) complexes on Fe, Mn oxides and humic acid. Chem Geol 185:33–49. https://doi.org/10.1016/S0009-2541(01)00393-X

Reith F, Lengke MF, Falconer D, Craw D, Southam G (2007) The geomicrobiology of gold. ISME J 1:567–584. https://doi.org/10.1038/ismej.2007.75

Rona PA (1984) Hydrothermal mineralization at seafloor spreading centers. Earth Sci Rev 20:1–104. https://doi.org/10.1016/0012-8252(84)90080-1

Rose AW (1976) The effect of cuprous chloride complexes in the origin of red-bed copper and related deposits. Econ Geol 71:1036–1048. https://doi.org/10.2113/gsecongeo.71.6.1036

Roy S (1992) Environments and processes of manganese deposition. Econ Geol 87:1218–1236. https://doi.org/10.2113/gsecongeo.87.5.1218

Sajih M, Bryan ND, Livens FR, Vaughan DJ, Descostes M, Phrommavanh V, Nos J, Morris K (2014) Adsorption of radium and barium on goethite and ferrihydrite: A kinetic and surface complexation modelling study. Geochim Cosmochim Acta 146:150–163. https://doi.org/10.1016/j.gca.2014.10.008

Schippers A, Jozsa P, Sand W (1996) Sulfur chemistry in bacterial leaching of pyrite. Appl Environ Microbiol 62:3424–3431. https://doi.org/10.1128/aem.62.9.3424-3431.1996

Schwertmann U, Murad E (1983) Effect of pH on the formation of goethite and hematite from ferrihydrite. Clays Clay Min 31:277–284. https://doi.org/10.1346/CCMN.1983.0310405

Sharkey JB, Lewin SZ (1971) Conditions governing the formation of atacamite and paratacamite. Am Mineral 56:179–192

Smith D, Cann J, Escartín J (2006) Widespread active detachment faulting and core complex formation near 13°N on the Mid-Atlantic Ridge. Nature 442:440–443. https://doi.org/10.1038/nature04950

Smith DK, Escartín J, Schouten H, Cann JR (2008) Fault rotation and core complex formation: Significant processes in seafloor formation at slow-spreading mid-ocean ridges (Mid-Atlantic Ridge, 13°–15°N). Geochem Geophys Geosyst 9:Q03003. https://doi.org/10.1029/2007GC001699

Standish CD, Milton JA, Page TM, Brown RM, Douglas D, Paul B, Schlatt L, Foster GL (2024) 2D geochemical imaging of biogenic marine carbonates using LA-TOF-ICP-MS at 1 and 2 µm pixel resolution. Chem Geol 670:122438. https://doi.org/10.1016/j.chemgeo.2024.122438

Sugiyama I, Halevy I (2024) Long-term interaction of metals and phosphate with ferrihydrite in artificial seawater and implications for past and present environments. Chem Geol 670:122448. https://doi.org/10.1016/j.chemgeo.2024.122448

Sun SS, McDonough WF (1989) Chemical and isotopic systematics of oceanic basalts: Implications for mantle composition and processes. Geol Soc Lond Spec Publ 42:313–345. https://doi.org/10.1144/GSL.SP.1989.042.01.19

Swedlund PJ, Sivaloganathan S, Miskelly GM, Waterhouse GIN (2011) Assessing the role of silicate polymerization on metal oxyhydroxide surfaces using X-ray photoelectron spectroscopy. Chem Geol 285:62–69. https://doi.org/10.1016/j.chemgeo.2011.02.022

Sylvan JB, Toner BM, Edwards KJ (2012) Life and death of deep-sea vents: Bacterial diversity and ecosystem succession on inactive hydrothermal sulfides. mBio 3:e00279–e00211. https://doi.org/10.1128/mBio.00279-11

Toner B, Santelli C, Marcus M, Wirth R, Chan C, McCollom T, Bach W, Edwards K (2009) Biogenic iron oxyhydroxide formation at Mid-Ocean Ridge hydrothermal vents: Juan de Fuca Ridge. Geochim Cosmochim Acta 73:388–403. https://doi.org/10.1016/j.gca.2008.09.035

Tronc E, Belleville P, Jolivet JP, Livage J (1992) Transformation of ferric hydroxide into spinel by iron(II) adsorption. Langmuir 8:313–319. https://doi.org/10.1021/la00037a057

van der Maaten LJP, Hinton GE (2008) Visualizing high-dimensional data using t-SNE. J Mach Learn Res 9:2579–2605

Vu HP, Shaw S, Brinza L, Benning LG (2013) Partitioning of Pb(II) during goethite and hematite crystallization: Implications for Pb transport in natural systems. Appl Geochem 39:119–128. https://doi.org/10.1016/j.apgeochem.2013.10.001

Webster JG (1986) The solubility of gold and silver in the system Au–Ag–S–O2–H2O at 25°C and 1 atm. Geochim Cosmochim Acta 50:1837–1845. https://doi.org/10.1016/0016-7037(86)90242-5

Webster JG, Mann AW (1984) The influence of climate, geomorphology and primary geology on the supergene migration of gold and silver. J Geochem Explor 22:21–42. https://doi.org/10.1016/0375-6742(84)90004-9

Wickham H (2016) ggplot2: Elegant graphics for data analysis. Springer, New York. https://doi.org/10.1007/978-3-319-24277-4

Wickham H, Bryan J (2023) Readxl: read excel files. https://readxl.tidyverse.org , https://github.com/tidyverse/readxl

Wickham H, François R, Henry L, Müller K, Vaughan D (2023) Dplyr: a grammar of data manipulation. R package version 1.1.4. https://github.com/tidyverse/dplyr , https://dplyr.tidyverse.org

Woods TL, Garrels RM (1986) Phase relations of some cupric hydroxy minerals. Econ Geol 81:1989–2007. https://doi.org/10.2113/gsecongeo.81.8.1989

Yesares L, Saez R, Nieto JM, de Almodovar GR, Cooper S (2014) Supergene enrichment of precious metals by natural amalgamation in the Las Cruces weathering profile (Iberian Pyrite Belt, SW Spain). Ore Geol Rev 58:14–26. https://doi.org/10.1016/j.oregeorev.2013.10.004